

Naphthalenediimide/Formamidinium-Based Low-Dimensional Perovskites

Aditya Mishra,[○] Paramvir Ahlawat,[○] George C. Fish,[○] Farzaneh Jahanbakhshi,[○] Marko Mladenović, Masaud Almalki, Marco A. Ruiz-Preciado, María C. Gelvéz-Rueda, Dominik J. Kubicki, Pascal A. Schouwink, Vincent Dufoulon, Thomas Schneeberger, Artin Aslanzadeh, Ferdinand C. Grozema, Shaik M. Zakeeruddin, Jacques-Edouard Moser, Ursula Rothlisberger,* Lyndon Emsley,* Jovana V. Milić,* and Michael Grätzel*



Cite This: *Chem. Mater.* 2021, 33, 6412–6420



Read Online

ACCESS |



Metrics & More

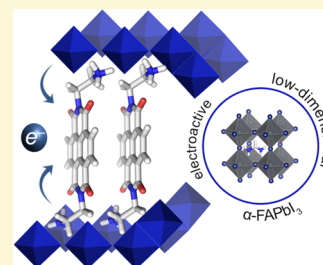


Article Recommendations



Supporting Information

ABSTRACT: Low-dimensional hybrid perovskites have emerged as promising materials for optoelectronic applications. Although these materials have already demonstrated enhanced stability as compared to their three-dimensional perovskite analogues, their functionality has been limited by the insulating character of the organic moieties that primarily play a structure-directing role. This is particularly the case for the layered (2D) perovskite materials based on formamidinium lead iodide (FAPbI₃) that remain scarce. We demonstrate a low-dimensional hybrid perovskite material based on a SPbI₄ composition incorporating an electroactive naphthalenediimide (NDI) moiety as an organic spacer (S) between the perovskite slabs and evidence the propensity of the spacer to stabilize the α -FAPbI₃ perovskite phase in hybrid low-dimensional SFA_{*n*-1}Pb_{*n*}I_{3*n*+1} perovskite compositions. This has been investigated by means of solid-state nuclear magnetic resonance spectroscopy in conjunction with molecular dynamics simulations and density functional theory calculations. Theoretical calculations suggest an electronic contribution of the organic spacer to the resulting optoelectronic properties, which was confirmed by transient absorption spectroscopy. We have further analyzed these materials by time-resolved microwave conductivity measurements, revealing challenges for their application in photovoltaics.



INTRODUCTION

Hybrid perovskites are one of the leading thin-film materials for optoelectronics.^{1–3} They are defined by the AMX₃ formula, where A represents the central A cation (commonly methylammonium (MA), formamidinium (FA) or Cs⁺), M the divalent metal (mainly Pb²⁺ and Sn²⁺), and X the halide (I⁻, Br⁻, or Cl⁻).¹ Despite their extraordinary optoelectronic properties, the challenges associated with stability hamper their commercial applications.² This obstacle stimulated the development of layered two-dimensional (2D) perovskite materials that incorporate hydrophobic organic cations between inorganic perovskite slabs.^{4,5} They form structures that can be expressed by S'₂A_{*n*-1}Pb_{*n*}X_{3*n*+1} and SA_{*n*-1}Pb_{*n*}X_{3*n*+1} formulas, where S' and S are either mono- or bifunctional organic spacers, respectively. Although this class of materials demonstrates enhanced stabilities against the environmental factors, the resulting performances remain inferior as compared to conventional three-dimensional (3D) hybrid perovskites.^{4,5} One of the underlying reasons for this limitation relates to the insulating character of the organic moieties that have been employed to date,⁴ which form natural quantum well structures with organic moieties as barriers to charge extraction (Figure 1a, top). This role can be tailored by introducing functional electroactive organic moieties as spacer units, which could

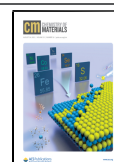
change their electronic structures (Figure 1a, bottom).⁵ Although the potential for this approach has been demonstrated theoretically, practical realizations of functional low-dimensional perovskites remain scarce.^{6–9} Moreover, the effort for the development of layered 2D hybrid perovskites and other low-dimensional (e.g., one-dimensional, 1D) analogues is predominantly focused on MA-based perovskite compositions, whereas FA-based analogues are underrepresented despite their higher thermal stability.^{10–14} One of the underlying reasons is that FAPbI₃ exists in two forms, the room-temperature-thermodynamically-stable yellow δ -FAPbI₃ and the photoactive α -FAPbI₃ phase.^{10,15} Stabilizing the α -FAPbI₃ perovskite phase hence remains an ongoing challenge that could further stimulate optoelectronic applications, particularly in conjunction with electroactive spacer moieties.⁶

Herein, we demonstrate low-dimensional hybrid perovskite materials based on an SFA_{*n*-1}Pb_{*n*}I_{3*n*+1} composition that

Received: May 12, 2021

Revised: July 21, 2021

Published: August 11, 2021



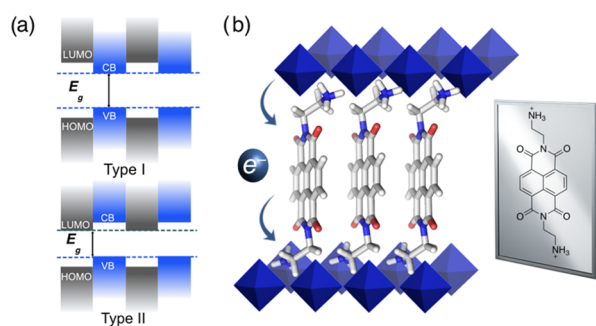


Figure 1. (a) Schematic representation of the electronic structure based on typical Type I (top) and Type II (bottom) quantum well structures of layered perovskites with the gray area representing the HOMO and LUMO levels of the organic spacer and blue area the band edges of the inorganic slabs. (b) Schematic representation of the layered perovskite material (left) incorporating electroactive NDIEA-based moieties (right) used in this study. NDIEA = 2,2'-(1,3,6,8-tetraoxo-1,3,6,8-tetrahydrobenzo[*lmn*][3,8]phenanthroline-2,7-diyl)-bis(ethylammonium); HOMO = highest occupied molecular orbital; LUMO = lowest unoccupied molecular orbital; CB = conduction band; VB = valence band.

incorporate electroactive naphthalenediimide (NDI)^{16–19} units as spacer moieties (S) that are linked to the perovskite via ethylammonium anchoring groups (Figure 1b). A comparable system has been described by Proppe et al. based on MA and MA/FA cation compositions, suggesting low-dimensional phase formation.¹⁸ We provide a comprehensive analysis of the FA-based hybrid perovskite materials by means of molecular dynamics (MD) simulations and density functional theory (DFT) calculations that reveal the capacity to form 2D perovskite structures in which spacer orbitals actively contribute to the band edge, which was complemented with the experimental characterization of the corresponding films. We demonstrate that low-dimensional perovskite phases contribute to stabilizing the α -FAPbI₃ phase, which was evidenced by solid-state NMR spectroscopy. Moreover, we evidence electron transfer between the perovskite slabs and the organic spacer with transient absorption spectroscopy. We further probe the utility of hybrid composites by time-resolved microwave conductivity measurements, which reveal obstacles to their application due to a high level of structural disorder with respect to the low-dimensional (1D, 2D) and compositional (*n*) phase mixtures and their orientation in the material.

EXPERIMENTAL SECTION

Materials and Methods. Reactions were performed in standard glassware under an ambient atmosphere unless otherwise specified. Commercially available chemicals were used without further purification. Purification was performed using dry flash chromatography on SiO₂ 60 (particle size 0.040–0.063 mm, 230–400 mesh) at a maximum head pressure of 0.2 bar. The procedures are detailed in the Supporting Information (SI) Sections S1 and S2.

Synthesis of the Spacer. *tert*-Butyl-*N*-(2-aminoethyl)carbamate (1.5 mL, 37 mmol) was added to a suspension of naphthalene-1,4,5,8-tetracarboxylic dianhydride (1.00 g, 3.73 mmol) in DMF (30 mL). The mixture was stirred for 15 h at 75 °C. The product was extracted by CH₂Cl₂, dried over anhydrous MgSO₄, and concentrated under vacuum. Dry flash chromatography (SiO₂, CH₂Cl₂/CH₃OH 9:1) yielded a di-*tert*-butyl((1,3,6,8-tetraoxo-1,3,6,8-tetrahydrobenzo[*lmn*]-[3,8]phenanthroline-2,7-diyl)bis(ethane-2,1-diyl))dicarbamate intermediate (1.7 g, 83%) as an orange solid. HI (1.67 mL, 12.6 mmol, 57%) was added to its suspension (1.7 g, 3.08 mmol) in ethanol (15 mL) at 0 °C. The mixture was stirred for 12 h and the resulting

solution was concentrated, resuspended in diethyl ether (10 mL), filtered, washed with diethyl ether and isopropanol, and dried under vacuum to yield 2,2'-(1,3,6,8-Tetraoxo-1,3,6,8-tetrahydrobenzo[*lmn*]-[3,8]phenanthroline-2,7-diyl)bis(ethylammonium) iodide (NDIEAI₂) (0.7 g, 75%) as a yellow solid. ¹H NMR (400 MHz, (CD₃)₂SO): δ = 8.74 (s, 4H), 7.81 (s, 6H), 4.35 (t, *J* = 5.9 Hz, 4H), 3.20 (q, *J* = 5.9 Hz, 4H) ppm; ¹³C NMR (101 MHz, (CD₃)₂SO): δ = 163.73, 130.88, 127.06, 126.68, 38.35, 37.98 ppm; HRMS (ESI+/QTOF): *m/z* (%) 353.1241 (100, [M]⁺, calcd for C₁₈H₁₇N₄O₄⁺: 353.1244); (ESI-/QTOF): *m/z* (%) 126.9055 (100, [M]⁻, calcd for I⁻: 126.9050).

Synthesis of (NDIEA)PbI₄ and (NDIEA)FA_{*n*-1}Pb_{*n*3*n*+1} Thin Films. The perovskite precursor solutions were prepared by dissolving stoichiometric amounts of PbI₂ (TCI), FAI (GreatCell Solar), and NDIEAI₂ according to the molecular formula of (NDIEA)-FA_{*n*-1}Pb_{*n*3*n*+1} in the dimethyl sulfoxide (DMSO)/*N,N*-dimethylformamide (DMF) mixture (1:4, v/v) at 0.4 M concentration of PbI₂. The perovskite film was deposited by spin-coating at 5000 rpm for 20 s (ramp rate 2000 rpm s⁻¹) on the glass substrates. The films were then annealed at 150 °C for 15 min. The preparation of the perovskite layer was carried out in a dry air-filled glove box with a relative humidity of <2%.

Mechanosynthesis of Perovskite Powders. Mechano-synthesis of perovskite powders was performed by grinding the reactants in an electric ball mill (Retsch Ball Mill MM-200) using a grinding jar (10 mL) and a ball (ø10 mm) for 30 min at 25 Hz. The powders were packed into 3.2 mm zirconia rotors and annealed at 150 °C for 15 min to reproduce the thin-film synthetic procedure, before transferring into the probe. The measurements were carried out under a dry nitrogen atmosphere.

Solution NMR Spectra. Solution NMR spectra (Figures S1–S2, SI) were recorded on a Bruker DRX 400 instrument operating at 400 MHz at 298 K. ¹³C NMR spectra were recorded on a Bruker DRX 400 operating at 100 MHz. Multiplicities are reported as follows: bs (broad singlet), s (singlet), d (doublet), and m (multiplet). Chemical shifts δ (ppm) were referenced to the internal solvent signals.

X-ray Diffraction Patterns. X-ray diffraction (XRD) patterns were recorded on an X'Pert MPD PRO (PANalytical) diffractometer equipped with a ceramic tube providing Ni-filtered (Cu anode, λ = 1.54060 Å) radiation and an RTMS X'Celerator (PANalytical) system. The measurements were performed in the BRAGG-BRENTANO geometry. The samples were mounted without further modification and the automatic divergence slit (10 mm) and beam mask (10 mm) were adjusted to the dimensions of the films.

Grazing Incidence Wide-Angle X-ray Scattering. Grazing incidence wide-angle X-ray scattering (GIWAXS) of (NDIEA)-FA_{*n*-1}Pb_{*n*3*n*+1} thin films on glass slides was measured at a 2° incidence angle with a D8 Discover Plus TXS (Bruker) equipped with rotating anode (Cu), a Dectris Eiger2 2D detector, and a point-collimated beam of approx. 300 μ m, at a power of 5.4 kW.

Scanning Electron Microscopy. Scanning electron microscopy (SEM) images were recorded using a high-resolution scanning electron microscope (Gemini-SEM 300). An electron beam accelerated to 3 kV was used with an in-lens detector. The images were measured with the perovskite infiltrated mp-TiO₂ films supported by FTO.

UV–Vis Absorption Measurements. UV–vis absorption measurements of (NDIEA)FA_{*n*-1}Pb_{*n*3*n*+1} films were performed using a Varian Cary5 UV–visible spectrophotometer.

Steady-State Photoluminescence. Steady-state photoluminescence (PL) spectra were recorded by exciting the layered perovskite films deposited onto glass slides. The emission between 460 and 830 nm was recorded with a Fluorolog 322 spectrometer (Horiba Jobin Yvon iHr320 and a CCD) within with a bandpass of 5 nm upon excitation at 420 nm with a bandpass of 5 nm. The samples were mounted at 60° and emission was recorded at 90° from the incident beam path.

Solid-State NMR Spectroscopy. Solid-state nuclear magnetic resonance (NMR) spectroscopy for ¹H (900 MHz) and ¹³C (225 MHz) was performed at a low temperature on a Bruker Avance Neo 21.1 T spectrometer equipped with a 3.2 mm low-temperature

CPMAS probe. ^{14}N (36.1 MHz) magic angle spinning (MAS) spectra were recorded on a Bruker Avance III 11.7 T spectrometer equipped with a 3.2 mm CPMAS probe. ^1H and ^{13}C chemical shifts were referenced to solid adamantane ($\delta_{\text{H}} = 1.91$ ppm and $\delta_{\text{C}} = 29.45$ (CH) and 38.48 (CH₂) ppm) at 298 K. ^{14}N spectra were referenced to solid NH_4Cl (0 ppm) at 298 K. A recycle delay of 0.3 s was used for the ^{14}N measurements.

Transient Absorption Spectra. Transient absorption (TA) spectra were measured using a femtosecond (fs) pump–probe spectrometer based on an amplified Ti:sapphire laser (Clark-MXR, CPA-2001) delivering 778 nm pulses with a pulse width of 150 fs and a repetition rate of 1 kHz. For excitation at 510 nm, the pump beam was generated by passing a portion of the fundamental beam through a two-stage non-collinear optical parametric amplifier (NOPA-Plus, Clark-MXR) resulting in an excitation wavelength of 510 nm. For excitation at 390 nm, the fundamental beam was passed through a BBO ($\beta\text{-BaB}_2\text{O}_4$) crystal in order to generate the second harmonic at 390 nm. The probe beam was a broadband white light continuum generated by passing part of the fundamental beam through a 5 mm thick oscillating CaF_2 plate. The pump and probe beams were set at magic-angle polarization and were spatially and temporally overlapping with respect to one another using a delay stage. A chopper, set at 500 Hz, was used to modulate the frequency of the pump beam, allowing for the absorption with and without the pump to be obtained. The probe beam was split before the sample into a reference and signal beam in order to account for shot-to-shot variations. The signal and reference beams were dispersed in a grating spectrograph (SpectraPro 2500i, Princeton Instruments) and detected at 1 kHz by a 512×58 pixel back-thinned charge-coupled device camera (Hamamatsu S07030-0906).

Density Functional Theory Calculations of the Spacer Moiety. Density functional theory (DFT) calculations of the spacer moiety were conducted with the Gaussian 09 Rev. D suite of programs.^{20,21} The geometry optimizations were performed at the B3LYP/6-31G(d) level of theory (Figure 1).

Molecular Dynamics Simulations and Density Functional Theory Calculations of Perovskite Structures. A detailed description of the molecular dynamics (MD) simulations and DFT calculations procedure are provided in the Supporting Information Sections S3 and S4, respectively.

RESULTS AND DISCUSSION

We investigate hybrid perovskite materials incorporating naphthalenediimide (NDI) moieties, employed to facilitate electron transport, which is functionalized with two ethylenammonium linkers as anchoring groups for inorganic perovskite slabs that form 2,2'-(1,3,6,8-tetraoxo-1,3,6,8-tetrahydrobenzo[*lmn*][3,8]phenanthroline-2,7-diyl)bis-(ethylammonium) (NDIEA; Figure 1b). This system is envisioned to form Dion–Jacobson-like ($\text{SFA}_{n-1}\text{Pb}_n\text{I}_{3n+1}$) perovskite phases ($n = 1-3$)²²⁻²⁷ and we thus studied these nominal compositions of the materials where $\langle n \rangle$ refers to the stoichiometry. We have primarily focused on lower compositional representatives ($\langle n \rangle = 1-3$) as $\langle n \rangle = 1$ compositions are known to form better defined 2D phases, whereas $\langle n \rangle > 1$ compositions commonly form mixtures of different $\langle n \rangle$ 2D/3D phases.^{4,5,22,23,27} We analyzed the morphology, structural, and optoelectronic properties by a multi-technique approach including both theoretical and experimental analysis.

Molecular Design and Theoretical Analysis. We have based our investigation on NDI-based electron acceptors that are commonly used in organic electronics and supramolecular chemistry due to high electron affinity, good charge carrier mobility in the solid-state, and excellent thermal and oxidative stability.¹⁶⁻¹⁸ Since haloplumbates based on NDI are characterized by a high degree of structural disorder (i.e., formation of both 1D and 2D phases),^{18,19} we first assess the

possibility of NDIEA₂ to form layered (2D) perovskite structures by classical molecular dynamics (MD) simulations (more details are provided in Section S3 of the SI). We base the simulations on a supercell with a Dion–Jacobson structure by placing NDIEA moieties between layers of corner-sharing Pb–I octahedra of different compositions (the specific procedure is detailed in the SI).¹⁴ As a result, we obtain stable and highly ordered 2D perovskite structures from classical MD (Figure S3, SI) that were subsequently relaxed at the DFT level to evidence the propensity to form a well-defined Dion–Jacobson structure. We find that the structure adopts the conformation in which the Pb–I–Pb angles are close to 180° (Figure 2). Moreover, the NDIEA spacer

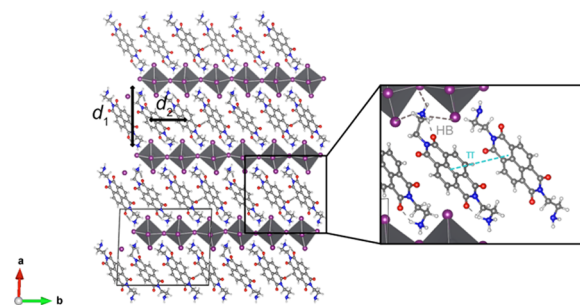


Figure 2. Simulated structure of (NDIEA)PbI₄ perovskites obtained by molecular dynamics simulations followed by DFT (PBEsol) calculations with characteristic interlayer distances (d_1 , d_2). Experimental details and other compositions are detailed in Sections S3 and S4 of the SI.

molecules are assembled via both hydrogen bonding and π – π interactions in the spacer layer (Figure 2, inset). As a result of these interactions, a rigid framework forms between the corresponding perovskite slabs (Figure 2).

To probe the templating effects of the spacer and the inorganic framework, we analyzed the average tilting angle between the octahedra (calculated as Pb–I–Pb angles), as well as the penetration depths of the spacers into the perovskite slabs by DFT calculations.^{14,28} We found that increasing the number of inorganic layers (n) leads to a decrease in the N...Pb distances and, consequently, an increase in the penetration depth.^{14,28-30} This leads to changes in the average Pb...Pb distances between opposite layers (d_1) as well as distances between the spacer moieties (d_2) (Figure 2; Figure S4 and Table S1, SI). Similar to the behavior of other layered hybrid perovskite systems, the interlayer distance (d_1) decreases upon deeper incorporation of the organic cation into the inorganic layer, evidencing templating effects through an interplay between the inorganic and organic layers that define the resulting structure.^{14,28} The spacers adopt a preferred conformation that remains unchanged during 5 ps of *ab initio* MD simulations at temperatures of 200, 300, and 400 K, which points to structural stability as a result of interactions in the spacer layer. Such structural preferences stimulated further investigation of these materials and their structural and optoelectronic properties.

Structural Properties. NDIEA-based films of $\text{SFA}_{n-1}\text{Pb}_n\text{I}_{3n+1}$ compositions ($\langle n \rangle = 1-3$; S = NDIEA; Figure 3a) are prepared by solution-processing of stoichiometric quantities of precursor materials followed by subsequent annealing at 150 °C for 15 min (as detailed in the Experimental Section, as well as Section S1, SI). The

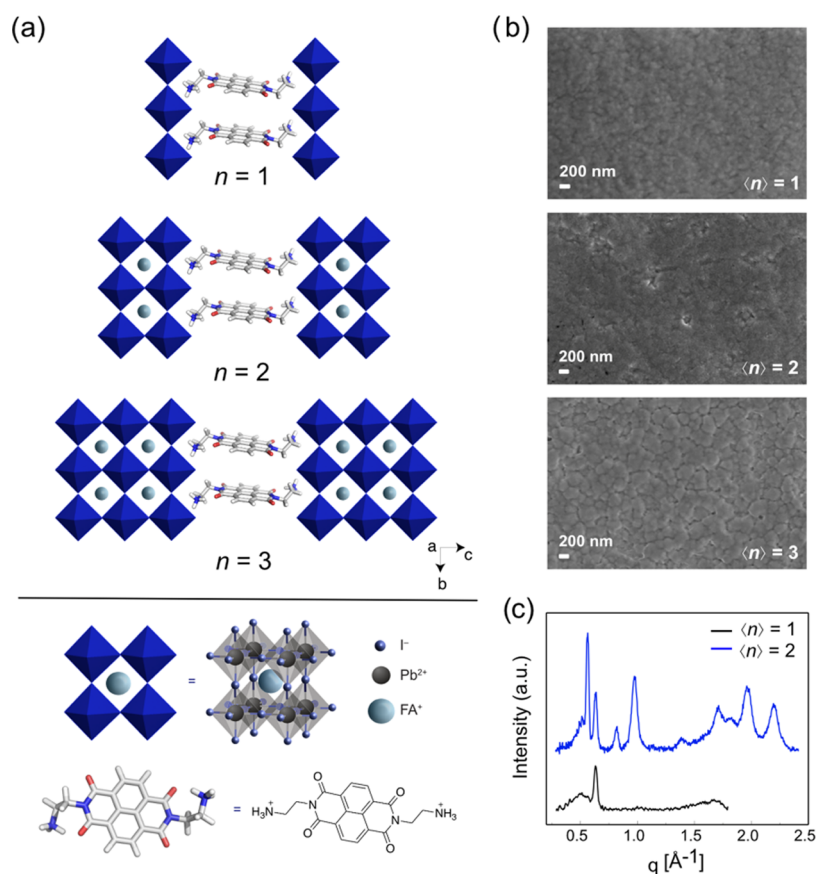


Figure 3. Structural representation and morphology. (a) Schematic of layered Dion–Jacobson structures based on $(\text{NDIEA})\text{FA}_{n-1}\text{Pb}_n\text{I}_{3n+1}$ compositions ($\langle n \rangle = 1-3$) with structural features of the compositional elements. The feasibility of these structures was confirmed theoretically, yet they were not experimentally evidenced since mixed low-dimensional phases form instead. (b) SEM images of perovskite films based on $(\text{NDIEA})\text{FA}_{n-1}\text{Pb}_n\text{I}_{3n+1}$ compositions ($\langle n \rangle = 1-3$). (c) Integrated diffraction patterns (from 2D GIWAXS images) for thin films of $(\text{NDIEA})\text{FA}_{n-1}\text{Pb}_n\text{I}_{3n+1}$ ($\langle n \rangle = 1-2$) compositions on microscope glass slides. Further details are provided in Section S5 and Figure S6 of the SI.

morphology of NDIEA-based films was investigated by scanning electron microscopy (SEM) of the film surface (Figure 3b). The SEM images show complete coverage of the surface of the film with relatively small nanometer-scale grain sizes that increase with increasing $\langle n \rangle$ up to 200 nm for $\langle n \rangle = 3$, with improving homogeneity.

The structural properties were further investigated by X-ray diffraction (XRD) measurements of thin films. XRD patterns (Figure S6, SI) of thin films show a signal at low reflection angles $2\theta < 10^\circ$, which we attribute to the low-dimensional perovskite phase associated with a d -spacing of around 10 Å ($\langle n \rangle = 1$) and 11–12 Å ($\langle n \rangle = 2$).^{14,22,31} However, integrated diffraction patterns of grazing incidence wide-angle X-ray scattering (GIWAXS) images (Figure S6, SI and Figure 3c) indicate a nearly complete absence of periodicity, even for $\langle n \rangle = 1$ phases, which is related to the low crystallinity under these experimental conditions. This is in accordance with the observations by Proppe et al. who have recently shown that films of NDI-based haloplumbates are highly disordered, containing 1D and 2D phases,¹⁸ although single crystals of 2D phases have also been reported.¹⁹ X-ray scattering measurements suggest low-dimensional phase formation for $\langle n \rangle = 1$ and $\langle n \rangle > 1$ compositions revealed by the signals in the q_z -range below 0.7 \AA^{-1} ($2\theta < 10^\circ$) that are commonly ascribed to the (00 l) planes (Figures 3c and S6, SI).^{13,14,18,19} Films based on the $\langle n \rangle = 1$ composition feature a signal at 0.63 \AA^{-1} , whereas those based on the $\langle n \rangle = 2$ composition show signals

at 0.56 and 0.52 \AA^{-1} that indicate distinct low-dimensional phases (Figure S6, SI). The signals associated with the $\langle n \rangle = 2$ composition more closely correspond to the calculated $n = 2$ phase (Section S4, SI). We do not observe other signals for $\langle n \rangle = 3$ compositions, which is in accordance with the previous reports suggesting that the formation of 2D FAPbI_3 -based $n > 2$ phases is rather challenging.²⁷ In addition, the lack of preferential orientation in the $\langle n \rangle = 1$ composition has been evidenced by GIWAXS (Section S5, Figure S6, SI) that display ring-shaped features with uniform angular intensity distribution that is associated with the random orientation of crystallites, whereas there is some preferential out-of-plane orientation for the distinct phase of the $\langle n \rangle = 2$ composition. Such differences in preferential orientation between the n phases are not uncommon and have been reported previously.^{14,27} Owing to this high degree of long-range disorder, we turn to solid-state NMR to investigate the local structure and atomic-level mixing.^{3,13,32–36}

We have performed echo-detected ^{14}N as well as $^1\text{H} \rightarrow ^{13}\text{C}$ and $^1\text{H} \rightarrow ^{15}\text{N}$ cross-polarization (CP) magic-angle spinning (MAS) NMR measurements (Figure 4). We compared the corresponding spectra of bulk mechanochemical α - FAPbI_3 as a model perovskite compound to those of the neat NDIEA I_2 and mechanochemical $(\text{NDIEA})\text{FA}_{n-1}\text{Pb}_n\text{I}_{3n+1}$ perovskite compositions (experimental details are provided in the Experimental Section and Section S1, SI). The ^{15}N CP NMR resonances revealed the presence of new environments in the spectral

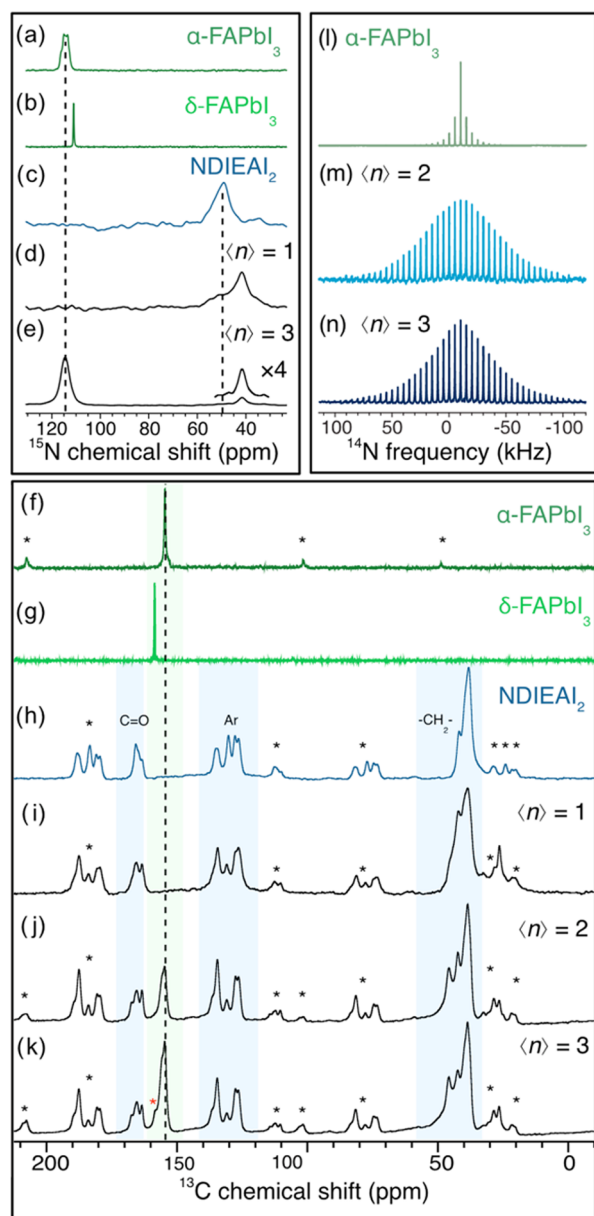


Figure 4. Structural properties determined by solid-state NMR spectroscopy. ^{15}N MAS NMR spectra at 21.1 T, 100 K, with 12.5 kHz MAS of (a) $\alpha\text{-FAPbI}_3$, (b) $\delta\text{-FAPbI}_3$, (c) neat NDIEAl_2 , and (d, e) $(\text{NDIEA})\text{FA}_{n-1}\text{Pb}_n\text{I}_{3n+1}$ ($\langle n \rangle = 1, 3$). ^{13}C CP solid-state MAS NMR spectra at 21.1 T, 100 K, with 12 kHz MAS of (f) $\alpha\text{-FAPbI}_3$, (g) $\delta\text{-FAPbI}_3$, (h) neat NDIEAl_2 , and (i–k) $(\text{NDIEA})\text{FA}_{n-1}\text{Pb}_n\text{I}_{3n+1}$ ($\langle n \rangle = 1, 2, 3$). ^{14}N MAS NMR spectra at 21.1 T, 100 K, with 12.5 kHz MAS of bulk (l) $\alpha\text{-FAPbI}_3$ and (m, n) $(\text{NDIEA})\text{FA}_{n-1}\text{Pb}_n\text{I}_{3n+1}$ ($\langle n \rangle = 2, 3$). Asterisks mark spinning sidebands, whereas the red asterisk in (k) indicates residual $\delta\text{-FAPbI}_3$.

region of both FA (100–120 ppm) and NDIEA (40–60 ppm) cations for all $(\text{NDIEA})\text{FA}_{n-1}\text{Pb}_n\text{I}_{3n+1}$ perovskite compositions (Figure 4a–e), which are indicative of the formation of new iodoplumbate phases containing FA/NDIEA moieties formed upon the atomic-level interaction of $-\text{NH}_3^+$ moieties and FAPbI_3 perovskite lattice through hydrogen bonding. A comparison with the neat NDIEAl_2 spacer precursor reveals full consumption of the spacer, as suggested by the disappearance of the spacer resonances at ca. 50 ppm (Figure 4c–e). The $\langle n \rangle = 2$ –3 compositions further indicate the stabilization of the $\alpha\text{-FAPbI}_3$ phase (Figure 4a,e) with the

corresponding signal at ca. 115 ppm. Similarly, the ^{13}C CP NMR spectra (Figure 4f–k) of the corresponding mechanochemical mixtures reveal the formation of new phases that can be associated with the presence of the NDIEA and FA cations in new environments that are closely related to the $\alpha\text{-FAPbI}_3$ phase, with a minor residual $\delta\text{-FAPbI}_3$ phase in the $\langle n \rangle = 3$ composition (Figure 4k). These environments may be ascribed to the interaction of the spacer with the surface of the PbI_2 and $\alpha\text{-FAPbI}_3$ perovskites in a low-dimensional perovskite phase, which yields ^{13}C and ^{15}N resonances that are not substantially shifted from the neat components, suggesting that the large NDIEA cation does not incorporate into the A-cation site of the 3D perovskite lattice and remains at the surface. As a result of this interaction, changes in the underlying crystallographic symmetry can be observed, as revealed by ^{14}N NMR spectra (Figure 4l–n). The width of the ^{14}N spinning sideband (SSB) manifolds is related to the local symmetry of FA reorienting inside the perovskite cavity.^{13,32–36} In this regard, narrower ^{14}N SSB manifolds indicate a higher symmetry of the local environment that is closer to the cubic one. The comparison of the ^{14}N MAS NMR spectra of $\alpha\text{-FAPbI}_3$ and $\langle n \rangle = 2, 3$ perovskite compositions feature an SSB pattern that is broader than the neat $\alpha\text{-FAPbI}_3$, which suggests lowering of symmetry upon low-dimensional structure formation. In summary, solid-state NMR spectroscopy measurements confirm the formation of new structures by the interaction between NDIEAl_2 and either PbI_2 (for $\langle n \rangle = 1$ compositions) or $\alpha\text{-FAPbI}_3$ (for $\langle n \rangle = 2, 3$ compositions) that could be ascribed to the formation of a low-dimensional phase and stabilization of the black $\alpha\text{-FAPbI}_3$ perovskite phase, which is relevant for the optoelectronic properties.

Optoelectronic Properties. To further understand hybrid materials formed with NDIEA, their optoelectronic properties were assessed by means of UV–vis absorption spectroscopy. The gradual color change from dark yellow to black with the increasing number of inorganic layers $\langle n \rangle$ is indicative of the possible effect of the spacer on the stabilization of the black $\alpha\text{-FAPbI}_3$ perovskite phase (Figure 5a). UV–vis absorption spectra for films with $\langle n \rangle = 1$ –3 compositions (Figure 5b) shows an excitonic peak at around 400 nm for the $\langle n \rangle = 1$ compositions, which is typical for low-dimensional perovskites.^{5,14} Moreover, additional absorption peaks are apparent in the region between 500 and 650 nm (Figure 5b), which might be related to the electronic exchange between the organic spacer and the inorganic slabs.^{18,19} This further corroborates with the significant quenching of the steady-state PL spectra (Figure S8, SI), in accordance with the observations of Proppe et al.¹⁸ For $\langle n \rangle = 2$ compositions, a much broader absorption spectrum is observed with an onset above 700 nm, which is suggestive of the formation of mixed 3D perovskite phases. Possible excitonic peaks corresponding to various n phases may be visible at higher wavelengths (500–650 nm, Figure 5b, dashed lines), suggestive of potential 2D subphase formation. However, broad absorption signals are in accordance with the structural disorder that can be attributed to mixed phase formation.

To understand the optical properties, the band gaps of the DFT-optimized $(\text{NDIEA})\text{FA}_{n-1}\text{Pb}_n\text{I}_{3n+1}$ structures were calculated (details are provided in Section S4 of the SI). The calculated band gap for $(\text{NDIEA})\text{PbI}_4$ is found to be in a reasonable agreement with the experimental optical gap estimates of around 2.37 eV (Table S2, SI and Figure 5b). The band gap is lower as compared to other Dion–Jacobson

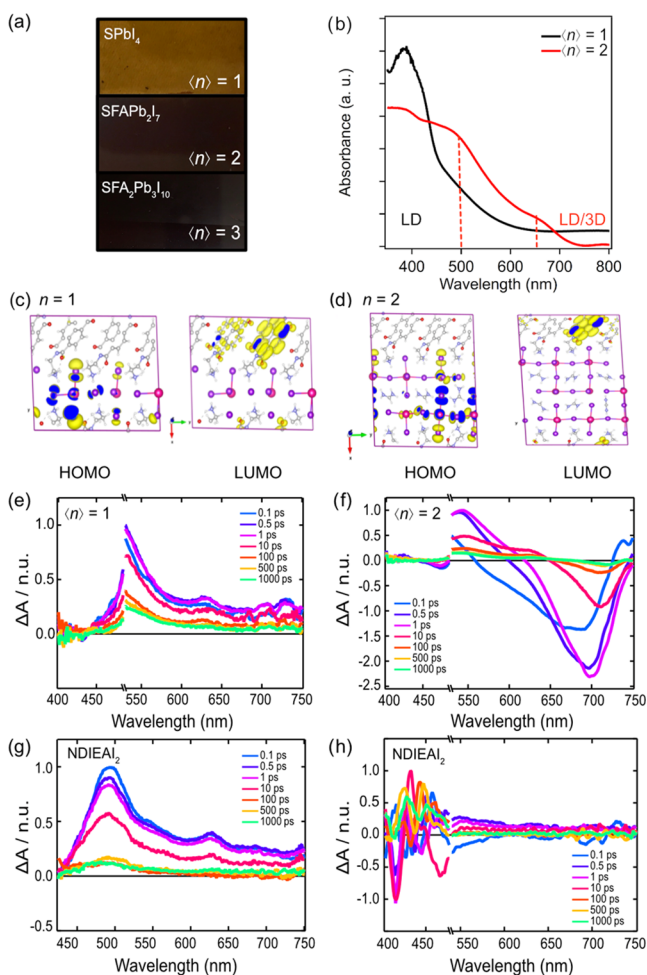


Figure 5. Optical properties. (a) Images of the perovskite films on microscope glass slides and (b) UV-vis absorption spectra for (NDIEA) $FA_{n-1}Pb_nI_{3n+1}$ compositions ($\langle n \rangle = 1-2$). (c, d) Calculated molecular orbitals (highest occupied molecular orbital, HOMO and lowest unoccupied molecular orbitals, LUMO) for (c) $n = 1$ and (d) $n = 2$ phases. The partial density of states and further details are provided in the SI, Section S4. (e-h) Transient absorption spectra for thin films of the (e, f) (NDIEA) $FA_{n-1}Pb_nI_{3n+1}$ composition ($\langle n \rangle = 1-2$) and (g, h) NDIEA I_2 : upon excitation at 510 nm (e, f, h) and 400 nm (g). The spectral shape does not change over time and the generated species are long-lived.

systems, which could be the result of either the symmetry being closer to cubic that would enhance orbital overlaps or a more substantial overlap between the organic and inorganic phases. Moreover, orbitals of the organic moieties directly contribute to the bottom of the conduction band (CB) (Figures S3c,d and S5, SI), resulting in significant lowering of the CB with respect to the inorganic layer, in accordance with the Type-II quantum well structure (Figure 1b, bottom). The projected densities of states (Figure S5, SI) corroborate the contribution of the organic moieties to the band edges for all perovskite compositions. Furthermore, calculated orbitals (Figures S3c,d and S5, SI) indicate localization of the bottom of the CB as well as higher states on the NDIEA spacer moieties, while the top of the valence band (VB) is delocalized over the inorganic part. As a result, the effective masses in the in-plane directions decrease upon increasing n for both electrons and holes, while significantly higher values for electrons prevail in the perpendicular direction to the inorganic

layer (Table S2, SI). Although some of the in-plane calculated effective hole masses tend to be somewhat lower than those of 1,4-phenyldimethan ammonium (PDMA)-based Dion-Jacobson structures,¹⁴ the effective masses for electrons are significantly increased with respect to other 2D perovskites³⁷ due to the localized nature of the spacer-dominated CB, which could affect charge transport in these hybrid materials.

The electronic properties and interactions between the organic spacer and the perovskite slabs were thereby probed by transient absorption (TA) spectroscopy (Figures 5e-g and S7, Section S6 SI). Upon excitation of the films with the (NDIEA) $FA_{n-1}Pb_nI_{3n+1}$ composition ($\langle n \rangle = 1-2$) at 510 nm a positive feature appears within the first 100 fs between 450 and 550 nm (Figure 5e,f). The TA spectra of the neat NDIEA film at 400 nm (Figure 5g) confirm that this feature seen in the spectra of the hybrid material corresponds to the formation of NDIEA-based radical anions.¹⁶⁻¹⁸ This is, however, not observed in the NDIEA-based films upon excitation at 510 nm (Figure 5h), confirming that it originates from the electron transfer between the organic spacer and the perovskite layers. This exchange process does not take place in systems incorporating electronically inactive spacers, such as the PDMA-based systems (Figure S7, SI), which have been previously shown to form Dion-Jacobson perovskite phases.²³ Although the reference PDMA-based system also involves a bleach at 520 nm characteristic for layered 2D perovskites,¹⁸ we do not observe such a feature in the NDIEA-based films, which is likely covered by the signal at around 510 nm (Figures 5e,f and S7). The spectral shape does not change over time and the generated species are long-lived, in accordance with the formation of radical anions. Furthermore, the TA spectra of $\langle n \rangle = 2$ compositions reveal an additional bleaching signal in the 625-750 nm range that is characteristic for the 3D perovskite phase (Figure 5f).³⁸

Having evidenced a rapid charge transfer between the organic and the inorganic components of the hybrid composite, time-resolved microwave conductivity (TRMC) measurements were used to probe changes in the conductivity of hybrid perovskites by using high-frequency microwaves after the excitation by either a high energy electron pulse or a laser (Section S7, SI).^{7,9,14,39} The generated free charge carriers absorb part of the microwave power and this fraction of the absorbed microwave power (ΔG) is proportional to the change in conductivity of the material ($\Delta\sigma$), which, in turn, is defined as the product of charge mobility (μ) and quantum yield of free charge carrier formation (φ).³⁹ Therefore, TRMC upon laser photoexcitation was used to analyze films of approximately 200 nm thickness with different compositions ($\langle n \rangle = 1-3$; Figure S9, SI). The photoconductivity of $\langle n \rangle = 1$ compositions was rather low, accompanied by a long lifetime on the μ s timescale, while the photoconductivity was found to increase by 2 orders of magnitude for $\langle n \rangle = 2$ compared to $\langle n \rangle = 1$ compositions, and by another order of magnitude for $\langle n \rangle = 3$ as compared to the $\langle n \rangle = 2$ composition, with lower lifetimes than for $\langle n \rangle > 1$ systems (below 400 ns). In contrast to the predicted theoretical structures, the photoconductivity values are found to be lower for these materials compared to conventional layered perovskite phases,^{7,9,14} which is likely the result of the structurally disordered low-dimensional structures, as suggested by solid-state NMR and X-ray scattering measurements. The level of disorder may also be the result of stronger noncovalent interactions in the spacer layer, which could compromise its adaptability in the formation of 2D

perovskites, leading to mixed low-dimensional phases and their orientations.³⁷ In addition, the highly localized nature of the CB revealed by theoretical analysis is likely to affect the charge transport. This was further confirmed by trial tests of photovoltaic performances in conventional solar cell devices (detailed in Section S8, SI) that suggest lower performances under several conditions as compared to other 2D and 2D/3D perovskites (Tables S3–S5, Figure S10, SI). These limitations stimulate further investigations towards minimizing the level of disorder in the compositions with enhanced phase purity, which could enable the effective incorporation of such functional materials into other optoelectronic devices in the future.

CONCLUSIONS

We have investigated hybrid FA-based perovskites incorporating 2,2'-(1,3,6,8-tetraoxo-1,3,6,8-tetrahydrobenzo[*lmn*][3,8]-phenanthroline-2,7-diyl)bis(ethylammonium) (NDIEA) moieties to assess the possibility to develop low-dimensional perovskite materials with enhanced charge transport. Molecular dynamics simulations complemented by density functional theory calculations suggested the existence of well-defined Dion–Jacobson perovskite phases based on (NDIEA)-FA_{*n*-1}Pb_{*n*}I_{3*n*+1} (*n* = 1–3) compositions, which were analyzed experimentally in powders and thin films. X-ray scattering measurements and solid-state NMR spectroscopy confirmed the formation of low-dimensional phases and the stabilization of the black α -FAPbI₃ perovskite phase, yet with a higher level of structural disorder without exhibiting well-defined layered perovskites. Furthermore, DFT calculations predicted the formation of Type II quantum well structures in layered perovskites, which is assumed to contribute to the narrowing of the band gaps and facilitate charge transfer. However, the calculated effective masses for electron transport turn out to be significantly increased due to a highly localized nature of the spacer-centered bottom of the CB. Accordingly, transient absorption spectroscopy confirms the electronic exchange between the organic moieties and hybrid perovskite slabs that corroborates with the significant quenching of the steady-state PL spectra, whereas time-resolved microwave conductivity measurements reveal lower photoconductivity that is attributed to structural disorder in the mixed low-dimensional phases and highly localized nature of the bottom of the CB, which affect optoelectronic properties. This study thereby unravels critical features of these low-dimensional electron-transporting perovskites, stimulating further investigations to enable their utility in optoelectronics.

ASSOCIATED CONTENT

Supporting Information

The Supporting Information is available free of charge at <https://pubs.acs.org/doi/10.1021/acs.chemmater.1c01635>. Data presented here can be accessed at DOI:10.5281/zenodo.5172265 and it is available under the license CC-BY-4.0 (Creative Commons Attribution-ShareAlike 4.0 International) or from the corresponding authors upon request.

Materials and methods, structural data, molecular dynamics simulations, DFT calculations, X-ray scattering measurements, transient absorption spectroscopy, time-resolved microwave conductivity measurements, and photovoltaic performance (PDF)

AUTHOR INFORMATION

Corresponding Authors

Ursula Rothlisberger – Laboratory of Computational Chemistry and Biochemistry, École Polytechnique Fédérale de Lausanne, 1015 Lausanne, Switzerland; orcid.org/0000-0002-1704-8591; Email: ursula.roethlisberger@epfl.ch

Lyndon Emsley – Laboratory of Magnetic Resonance, École Polytechnique Fédérale de Lausanne, 1015 Lausanne, Switzerland; orcid.org/0000-0003-1360-2572; Email: lyndon.emsley@epfl.ch

Jovana V. Milić – Laboratory of Photonics and Interfaces, École Polytechnique Fédérale de Lausanne, 1015 Lausanne, Switzerland; Adolphe Merkle Institute, University of Fribourg, 1700 Fribourg, Switzerland; orcid.org/0000-0002-9965-3460; Email: jovana.milic@unifr.ch

Michael Grätzel – Laboratory of Photonics and Interfaces, École Polytechnique Fédérale de Lausanne, 1015 Lausanne, Switzerland; orcid.org/0000-0002-0068-0195; Email: michael.graetzel@epfl.ch

Authors

Aditya Mishra – Laboratory of Magnetic Resonance, École Polytechnique Fédérale de Lausanne, 1015 Lausanne, Switzerland

Paramvir Ahlawat – Laboratory of Computational Chemistry and Biochemistry, École Polytechnique Fédérale de Lausanne, 1015 Lausanne, Switzerland; orcid.org/0000-0003-2355-3663

George C. Fish – Photochemical Dynamics Group, École Polytechnique Fédérale de Lausanne, 1015 Lausanne, Switzerland

Farzaneh Jahanbakhshi – Laboratory of Computational Chemistry and Biochemistry, École Polytechnique Fédérale de Lausanne, 1015 Lausanne, Switzerland; orcid.org/0000-0001-7113-2746

Marko Mladenović – Laboratory of Computational Chemistry and Biochemistry, École Polytechnique Fédérale de Lausanne, 1015 Lausanne, Switzerland

Masaud Almalki – Laboratory of Photonics and Interfaces, École Polytechnique Fédérale de Lausanne, 1015 Lausanne, Switzerland

Marco A. Ruiz-Preciado – Laboratory of Photonics and Interfaces, École Polytechnique Fédérale de Lausanne, 1015 Lausanne, Switzerland

María C. Gelvéz-Rueda – Department of Chemical Engineering, Delft University of Technology, 2629 Delft, The Netherlands

Dominik J. Kubicki – Laboratory of Magnetic Resonance, École Polytechnique Fédérale de Lausanne, 1015 Lausanne, Switzerland; Laboratory of Photonics and Interfaces, École Polytechnique Fédérale de Lausanne, 1015 Lausanne, Switzerland; orcid.org/0000-0002-9231-6779

Pascal A. Schouwink – X-ray Diffraction and Surface Analytics, École Polytechnique Fédérale de Lausanne, 1951 Sion, Switzerland

Vincent Dufoulon – Laboratory of Photonics and Interfaces, École Polytechnique Fédérale de Lausanne, 1015 Lausanne, Switzerland

Thomas Schneeberger – Laboratory of Photonics and Interfaces, École Polytechnique Fédérale de Lausanne, 1015 Lausanne, Switzerland; X-ray Diffraction and Surface Analytics, École Polytechnique Fédérale de Lausanne, 1951 Sion, Switzerland

Artin Aslanzadeh – *Adolphe Merkle Institute, University of Fribourg, 1700 Fribourg, Switzerland*

Ferdinand C. Grozema – *Department of Chemical Engineering, Delft University of Technology, 2629 Delft, The Netherlands*; orcid.org/0000-0002-4375-799X

Shaik M. Zakeeruddin – *Laboratory of Photonics and Interfaces, École Polytechnique Fédérale de Lausanne, 1015 Lausanne, Switzerland*

Jacques-Edouard Moser – *Photochemical Dynamics Group, École Polytechnique Fédérale de Lausanne, 1015 Lausanne, Switzerland*; orcid.org/0000-0003-0747-4666

Complete contact information is available at:

<https://pubs.acs.org/10.1021/acs.chemmater.1c01635>

Author Contributions

○A.M., P.A., G.C.F., and F.J. contributed equally to this work. The manuscript was written by A.M. and J.V.M. through contributions of all authors. The research was conceptualized and coordinated by J.V.M., who performed the preliminary study and supervised the investigation. A.M. performed the solid-state NMR spectroscopy and data analysis with the support of D.J.K., whereas P.A. conducted molecular dynamics simulations. F.J. and M.M. performed the DFT calculations. M.A.R.-P. performed the photovoltaic device fabrication and characterization with the support of M.A., who performed additional film characterization. M.A. and P.A.S. performed the GIWAXS measurements and analysis. V.D. prepared thin films and performed their characterization by UV–vis absorption and PL spectroscopy. T.S. and A.A. synthesized and characterized the spacer and T.S. performed the mechanosynthesis, while G.C.F. and J.-E.M. performed transient absorption spectroscopy measurements and analysis. S.M.Z. was involved in the discussions. U.R., L.E., and M.G. directed the study. All authors have contributed to the manuscript and given approval to the final version.

Funding

This work is supported by the Swiss National Science Foundation Grants No. 193174, 200020 178860, 200021_175729, 200020_165863, NCCR-MUST, NRP70, and the SINERGIA interdisciplinary research program EPISODE, as well as the GRAPHENE Flagship Core 2 project of the European Commission H2020 Programme under contract 785219.

Notes

The authors declare no competing financial interest.

ACKNOWLEDGMENTS

J.V.M. acknowledges support from the Swiss National Science Foundation (SNSF) Grant No. 193174. M.G. is grateful for the financial support from the European Union's H2020 programme under grant agreement no. 785219. A.M., D.J.K., and L.E. are grateful for support from SNSF Grant No. 200020_178860. G.C.F. and J.-E.M. thank the SNSF (grant no. 200021_175729) and NCCR-MUST for financial support. U.R. acknowledges SNSF Grant No. 200020 165863, NCCR-MUST, NRP70, and the SINERGIA interdisciplinary research program EPISODE for funding, as well as the computing time from the Swiss National Supercomputing Centre (CSCS). The authors are grateful to Dr. Amita Ummadisingu (EPFL) for insightful discussions and Dr. Renana Gershoni-Poranne (ETH Zurich) for electrostatic potential surface mapping.

ABBREVIATIONS

CB, conduction band; DFT, density functional theory; GIWAXS, grazing incidence wide-angle X-ray scattering; HOMO, highest occupied molecular orbital; LUMO, lowest unoccupied molecular orbital; MD, molecular dynamics; NDI, naphthalenediimide; NDIEA, 2,2'-(1,3,6,8-tetraoxo-1,3,6,8-tetrahydrobenzo[*lmn*][3,8]phenanthroline-2,7-diyl)bis(ethanol-1-aminium); NMR, nuclear magnetic resonance; PDMA, 1,4-phenyldimethan ammonium; PL, photoluminescence spectroscopy; TAS, transient absorption spectroscopy; TRMC, time-resolved microwave conductivity; XRD, X-ray diffraction

REFERENCES

- (1) Grätzel, M. The Light and Shade of Perovskite Solar Cells. *Nat. Mater.* **2014**, *13*, 838–842.
- (2) Rong, Y.; Hu, Y.; Mei, A.; Tan, H.; Saidaminov, M. I.; Seok, S. I.; McGehee, M. D.; Sargent, E. H.; Han, H. Challenges for Commercializing Perovskite Solar Cells. *Science* **2018**, *361*, No. eaat8235.
- (3) Milić, J. V.; Kubicki, D. J.; Emsley, L.; Grätzel, M. Multifunctional Molecular Modulation for Efficient and Stable Hybrid Perovskite Solar Cells. *Chimia* **2019**, *73*, 317–323.
- (4) Saparov, B.; Mitzi, D. B. Organic–Inorganic Perovskites: Structural Versatility for Functional Materials Design. *Chem. Rev.* **2016**, *116*, 4558–4596.
- (5) Mao, L.; Stoumpos, C. C.; Kanatzidis, M. G. Two-Dimensional Hybrid Halide Perovskites: Principles and Promises. *J. Am. Chem. Soc.* **2019**, *141*, 1171–1190.
- (6) Maheshwari, S.; Savenije, T. J.; Renaud, N.; Grozema, F. C. Computational Design of Two-Dimensional Perovskites with Functional Organic Cations. *J. Phys. Chem. C* **2018**, *122*, 17118–17122.
- (7) Gélvez-Rueda, M. C.; Hutter, E. M.; Cao, D. H.; Renaud, N.; Stoumpos, C. C.; Hupp, J. T.; Savenije, T. J.; Kanatzidis, M. G.; Grozema, F. C. Interconversion between Free Charges and Bound Excitons in 2D Hybrid Lead Halide Perovskites. *J. Phys. Chem. C* **2017**, *121*, 26566–26574.
- (8) Passarelli, J. V.; Fairfield, D. J.; Sather, N. A.; Hendricks, M. P.; Sai, H.; Stern, C. L.; Stupp, S. I. Enhanced Out-of-Plane Conductivity and Photovoltaic Performance in *n* = 1 Layered Perovskites through Organic Cation Design. *J. Am. Chem. Soc.* **2018**, *140*, 7313–7323.
- (9) Herckens, R.; Van Gompel, W. T. M.; Song, W.; Gélvez-Rueda, M. C.; Maufort, A.; Ruttens, B.; D'Haen, J.; Grozema, F. C.; Aernouts, T.; Lutsen, L.; Vanderzande, D. Multi-Layered Hybrid Perovskites Templated with Carbazole Derivatives: Optical Properties, Enhanced Moisture Stability and Solar Cell Characteristics. *J. Mater. Chem. A* **2018**, *6*, 22899–22908.
- (10) Weller, M. T.; Weber, O. J.; Frost, J. M.; Walsh, A. Cubic Perovskite Structure of Black Formamidinium Lead Iodide, α -[HC(NH₂)₂]PbI₃, at 298 K. *J. Phys. Chem. Lett.* **2015**, *6*, 3209–3212.
- (11) Yan, J.; Fu, W.; Zhang, X.; Chen, J.; Yang, W.; Qiu, W.; Wu, G.; Liu, F.; Heremans, P.; Chen, H. Highly Oriented Two-Dimensional Formamidinium Lead Iodide Perovskites with a Small Bandgap of 1.51 eV. *Mater. Chem. Front.* **2018**, *2*, 121–128.
- (12) Wang, Z.; Lin, Q.; Chmiel, F. P.; Sakai, N.; Herz, L. M.; Snaith, H. J. Efficient Ambient-Air-Stable Solar Cells with 2D–3D Heterostructured Butylammonium-Caesium-Formamidinium Lead Halide Perovskites. *Nat. Energy* **2017**, *2*, No. 17135.
- (13) Milić, J. V.; Im, J.-H.; Kubicki, D. J.; Ummadisingu, A.; Seo, J.-Y.; Li, Y.; Ruiz Preciado, M. A.; Dar, M. I.; Zakeeruddin, S. M.; Emsley, L.; Grätzel, M. Supramolecular Engineering for Formamidinium-Based Layered 2D Perovskite Solar Cells: Structural Complexity and Dynamics Revealed by Solid-State NMR Spectroscopy. *Adv. Energy Mater.* **2019**, *9*, No. 1900284.
- (14) Gélvez-Rueda, M. C.; Ahlawat, P.; Merten, L.; Jahanbakhshi, F.; Mladenović, M.; Hinderhofer, A.; Dar, M. I.; Li, Y.; Dučinskas, A.; Carlsen, B.; Tress, W.; Ummadisingu, A.; Zakeeruddin, S. M.; Schreiber, F.; Hagfeldt, A.; Rothlisberger, U.; Grozema, F. C.; Milić, J.

V.; Graetzel, M. Formamidinium-Based Dion-Jacobson Layered Hybrid Perovskites: Structural Complexity and Optoelectronic Properties. *Adv. Funct. Mater.* **2020**, *30*, No. 2003428.

(15) Binek, A.; Hanusch, F. C.; Docampo, P.; Bein, T. Stabilization of the Trigonal High-Temperature Phase of Formamidinium Lead Iodide. *J. Phys. Chem. Lett.* **2015**, *6*, 1249–1253.

(16) Bhosale, S. V.; Jani, C. H.; Langford, S. Chemistry of Naphthalene Diimides. *Chem. Soc. Rev.* **2008**, *37*, 331–342.

(17) Al Kobaisi, M.; Bhosale, S. V.; Latham, K.; Raynor, A. M.; Bhosale, S. V. Functional Naphthalene Diimides: Synthesis, Properties, and Applications. *Chem. Rev.* **2016**, *116*, 11685–11796.

(18) Proppe, A. H.; Tremblay, M.-H.; Zhang, Y.; Yang, Z.; Quintero-Bermudez, R.; Kelley, S. O.; Barlow, S.; Marder, S. R.; Sargent, E. H. Naphthalenediimide Cations Inhibit 2D Perovskite Formation and Facilitate Subpicosecond Electron Transfer. *J. Phys. Chem. C* **2020**, *124*, 24379–24390.

(19) Li, X.; Yang, J.; Song, Z.; Chen, R.; Ma, L.; Li, H.; Jia, J.; Meng, J.; Li, X.; Yi, M.; Sun, X. Naphthalene Diimide Ammonium Directed Single-Crystalline Perovskites with “Atypical” Ambipolar Charge Transport Signatures in Two-Dimensional Limit. *ACS Appl. Energy Mater.* **2018**, *1*, 4467–4472.

(20) Foresman, J. B.; Frisch, A. *Exploring Chemistry with Electronic Structure Methods*, 2nd ed.; Gaussian, Inc., 1995; pp 1–335.

(21) Frisch, M. J.; Trucks, G. W.; Schlegel, G. W.; Scuseria, H. B.; Robb, G. E.; Cheeseman, M. A.; Scalmani, J. R.; Barone, G.; Mennucci, V.; Petersson, B.; Nakatsuji, G. A.; Caricato, H.; Li, M.; Hratchian, X.; Izmaylov, H. P.; Bloino, A. F.; Zheng, J.; Sonnenberg, G.; Hada, J. L.; Ehara, M.; Toyota, M.; Fukuda, K.; Hasegawa, R.; Ishida, J.; Nakajima, M.; Honda, T.; Kitao, Y.; Nakai, O.; Vreven, H.; Montgomery, T., Jr.; Peralta, J. A.; Ogliaro, J. E.; Bearpark, F.; Heyd, M.; Brothers, J. J.; Kudin, E.; Staroverov, K. N.; Kobayashi, V. N.; Normand, R.; Raghavachari, J.; Rendell, K.; Burant, A.; Iyengar, J. C.; Tomasi, S. S.; Cossi, J.; Rega, M.; Millam, N.; Klene, J. M.; Knox, M.; Cross, J. E.; Bakken, J. B.; Adamo, V.; Jaramillo, C.; Gomperts, J.; Stratmann, R.; Yazyev, R. E.; Austin, O.; Cammi, A. J.; Pomelli, R.; Ochterski, C.; Martin, J. W.; Morokuma, R. L.; Zakrzewski, K.; Voth, V. G.; Salvador, G. A.; Dannenberg, P.; Dapprich, J. J.; Daniels, S.; Farkas, A. D.; Foresman, O.; Ortiz, J. B.; Cioslowski, J. V.; Fox, D. J. *Gaussian D09*; Gaussian, Inc., 2009.

(22) Mao, L.; Ke, W.; Pedesseau, L.; Wu, Y.; Katan, C.; Even, J.; Wasielewski, M. R.; Stoumpos, C. C.; Kanatzidis, M. G. Hybrid Dion–Jacobson 2D Lead Iodide Perovskites. *J. Am. Chem. Soc.* **2018**, *140*, 3775–3783.

(23) Li, Y.; Milić, J. V.; Ummadisingu, A.; Seo, J.-Y.; Im, J.-H.; Kim, H.-S.; Liu, Y.; Dar, M. I.; Zakeeruddin, S. M.; Wang, P.; Hagfeldt, A.; Grätzel, M. Bifunctional Organic Spacers for Formamidinium-Based Hybrid Dion–Jacobson Two-Dimensional Perovskite Solar Cells. *Nano Lett.* **2019**, *19*, 150–157.

(24) Cohen, B.-E.; Li, Y.; Meng, Q.; Etgar, L. Dion–Jacobson Two-Dimensional Perovskite Solar Cells Based on Benzene Dimethan ammonium Cation. *Nano Lett.* **2019**, *19*, 2588–2597.

(25) Li, X.; Ke, W.; Traore, B.; Guo, P.; Hadar, I.; Kepenekian, M.; Even, J.; Katan, C.; Stoumpos, C. C.; Schaller, R. D.; Kanatzidis, M. G. Two-Dimensional Dion–Jacobson Hybrid Lead Iodide Perovskites with Aromatic Diammonium Cations. *J. Am. Chem. Soc.* **2019**, *141*, 12880–12890.

(26) Xu, Z.; Chen, M.; Liu, S. F. First-Principles Study of Enhanced Out-of-Plane Transport Properties and Stability in Dion–Jacobson Two-Dimensional Perovskite Semiconductors for High-Performance Solar Cell Applications. *J. Phys. Chem. Lett.* **2019**, *10*, 3670–3675.

(27) Milić, J. V.; Zakeeruddin, S. M.; Grätzel, M. Layered Hybrid Formamidinium Lead Iodide Perovskites: Challenges and Opportunities. *Acc. Chem. Res.* **2021**, *54*, 2729–2740.

(28) Ashari-Astani, N.; Jahanbakhshi, F.; Mladenović, M.; Alanazi, A. Q. M.; Ahmadabadi, I.; Ejtehadi, M. R.; Dar, M. I.; Grätzel, M.; Rothlisberger, U. J. Ruddlesden–Popper Phases of Methylammonium-Based Two-Dimensional Perovskites with 5-Ammonium Valeric Acid $\text{AVA}_2\text{MA}_{n-1}\text{Pb}_n\text{I}_{3n+1}$ with $n = 1, 2$, and 3 . *J. Phys. Chem. Lett.* **2019**, *10*, 3543–3549.

(29) Alanazi, A. Q.; Kubicki, D. J.; Prochowicz, D.; Alharbi, E. A.; Bouduban, M. E. F.; Jahanbakhshi, F.; Mladenović, M.; Milić, J. V.; Giordano, F.; Ren, D.; Alyamani, A. Y.; Albrithen, H.; Albadri, A.; Alotaibi, M. H.; Moser, J.-E.; Zakeeruddin, S. M.; Rothlisberger, U.; Emsley, L.; Grätzel, M. Atomic-Level Microstructure of Efficient Formamidinium-Based Perovskite Solar Cells Stabilized by 5-Ammonium Valeric Acid Iodide Revealed by Multi-Nuclear and Two-Dimensional Solid-State NMR. *J. Am. Chem. Soc.* **2019**, *141*, 17659–17669.

(30) Ahmad, S.; Fu, P.; Yu, S.; Yang, Q.; Liu, X.; Wang, X.; Wang, X.; Guo, X.; Li, C. Dion-Jacobson Phase 2D Layered Perovskites for Solar Cells with Ultrathin Stability. *Joule* **2019**, *3*, 794–806.

(31) Cao, D. H.; Stoumpos, C. C.; Farha, O. K.; Hupp, J. T.; Kanatzidis, M. G. 2D Homologous Perovskites as Light-Absorbing Materials for Solar Cell Applications. *J. Am. Chem. Soc.* **2015**, *137*, 7843–7850.

(32) Kubicki, D. J.; Prochowicz, D.; Hofstetter, A.; Pěchy, P.; Zakeeruddin, S. M.; Grätzel, M.; Emsley, L. Cation Dynamics in Mixed-Cation $(\text{MA})_x(\text{FA})_{1-x}\text{PbI}_3$ Hybrid Perovskites from Solid-State NMR. *J. Am. Chem. Soc.* **2017**, *139*, 10055–10061.

(33) Kubicki, D. J.; Prochowicz, D.; Hofstetter, A.; Zakeeruddin, S. M.; Grätzel, M.; Emsley, L. Phase Segregation in Cs-, Rb- and K-Doped Mixed-Cation $(\text{MA})_x(\text{FA})_{1-x}\text{PbI}_3$ Hybrid Perovskites from Solid-State NMR. *J. Am. Chem. Soc.* **2017**, *139*, 14173–14180.

(34) Kubicki, D. J.; Prochowicz, D.; Hofstetter, A.; Sasaki, M.; Yadav, P.; Bi, D.; Pellet, N.; Lewiński, J.; Zakeeruddin, S. M.; Grätzel, M.; Emsley, L. Formation of Stable Mixed Guanidinium–Methylammonium Phases with Exceptionally Long Carrier Lifetimes for High-Efficiency Lead Iodide-Based Perovskite Photovoltaics. *J. Am. Chem. Soc.* **2018**, *140*, 3345–3351.

(35) Bi, D.; Li, X.; Milić, J. V.; Kubicki, D. J.; Pellet, N.; Luo, J.; LaGrange, T.; Mettraux, P.; Emsley, L.; Zakeeruddin, S. M.; Grätzel, M. Multifunctional Molecular Modulators for Perovskite Solar Cells with over 20% Efficiency and High Operational Stability. *Nat. Commun.* **2018**, *9*, No. 4482.

(36) Hope, M. A.; Nakamura, T.; Ahlawat, P.; Mishra, A.; Cordova, M.; Jahanbakhshi, F.; Mladenović, M.; Runjhun, R.; Merten, L.; Hinderhofer, A.; Carlsen, B. I.; Kubicki, D. J.; Gershoni-Poranne, R.; Schneeberger, T.; Carbone, L. C.; Liu, Y.; Zakeeruddin, S. M.; Lewiński, J.; Hagfeldt, A.; Schreiber, F.; Rothlisberger, U.; Grätzel, M.; Milić, J. V.; Emsley, L. Nanoscale Phase Segregation in Supramolecular π -Templating for Hybrid Perovskite Photovoltaics from NMR Crystallography. *J. Am. Chem. Soc.* **2021**, *143*, 1529–1538.

(37) Jahanbakhshi, F.; Mladenović, M.; Dankl, M.; Boziki, A.; Ahlawat, P.; Rothlisberger, U. Organic Spacers in 2D Perovskites: General Trends and Structure-Property Relationships from Computational Studies. *Helv. Chim. Acta* **2021**, *104*, No. e2000232.

(38) Franco, C. V.; Mahler, B.; Cornaggia, C.; Gustavsson, T.; Cassette, E. Charge Carrier Relaxation in Colloidal FAPbI_3 Nanostructures Using Global Analysis. *Nanomaterials* **2020**, *10*, No. 1897.

(39) Gélvez-Rueda, M. C.; Fridriksson, M. B.; Dubey, R. K.; Jager, W. F.; van der Stam, W.; Grozema, F. C. Overcoming the Exciton Binding Energy in Two-Dimensional Perovskite Nanoplatelets by Attachment of Conjugated Organic Chromophores. *Nat. Commun.* **2020**, *11*, No. 1901.

Naphthalenediimide/Formamidinium–Based Low–Dimensional Perovskites

*Aditya Mishra^{‡, #}, Paramvir Ahlawat^{†, #}, George C. Fish^{#, #}, Farzaneh Jahanbakhshi^{†, #}, Marko Mladenović[†], Masaud Almalki[§], Marco A. Ruiz-Preciado[§], María C. Gelvéz-Rueda[‡], Dominik J. Kubicki^{§, ‡}, Pascal A. Schouwink[†], Vincent Dufoulon[§], Thomas Schneeberger[§], Artin Aslanzadeh[‡], Ferdinand C. Grozema[‡], Shaik M. Zakeeruddin[§], Jacques-Edouard Moser[#], Ursula Rothlisberger^{†, *}, Lyndon Emsley^{†, *}, Jovana V. Milić^{§, ‡, *}, and Michael Grätzel^{§, *}*

These authors contributed equally

[‡]Laboratory of Magnetic Resonance, École Polytechnique Fédérale de Lausanne, Switzerland; [†]Laboratory of Computational Chemistry and Biochemistry, École Polytechnique Fédérale de Lausanne, Switzerland; [§]Laboratory of Photonics and Interfaces, École Polytechnique Fédérale de Lausanne, Switzerland; [‡] Department of Chemical Engineering, Delft University of Technology, The Netherlands; [#]Photochemical Dynamics Group, École Polytechnique Fédérale de Lausanne, Switzerland; [†] X-ray Diffraction and Surface Analytics, École Polytechnique Fédérale de Lausanne, Switzerland; [‡] Adolphe Merkle Institute, University of Fribourg, Switzerland. *Correspondence: ursula.roethlisberger@epfl.ch; lyndon.emsley@epfl.ch; jovana.milic@unifr.ch; michael.gratzel@epfl.ch

Table of Contents

| | |
|--|----|
| S1. Materials and Methods | 2 |
| S2. Supplementary Structural Data..... | 3 |
| S3. Molecular Dynamics Simulations..... | 4 |
| S4. DFT Calculations..... | 6 |
| S5. X-Ray Scattering Measurements | 9 |
| S6. Transient Absorption Spectroscopy..... | 10 |
| S7. Time Resolved Microwave Conductivity Measurements..... | 11 |
| S8. Photovoltaic Performance..... | 12 |
| References..... | 14 |

Data presented here can be accessed at DOI:10.5281/zenodo.5172265 and it is available under the license CC-BY-4.0 (Creative Commons Attribution-ShareAlike 4.0 International) or from the corresponding authors upon request.

S1. Materials and Methods

*Spacer 2,2'-(1,3,6,8-tetraoxo-1,3,6,8-tetrahydrobenzo[*lmn*][3,8]phenanthroline-2,7-diyl)bis(ethan-1-aminium)* (NDIAI₂) *synthesis*: Boc-protected ethylene diamine (1.5 mL, 37 mmol) was added to a suspension of NDI anhydride (1.00 g, 3.73 mmol) in DMF (30 mL). The mixture was stirred for 15 h at 75 °C and the product was extracted by CH₂Cl₂, dried over anhydrous MgSO₄ and concentrated under vacuum. Dry flash chromatography (SiO₂, CH₂Cl₂/CH₂OH 9:1) yielded di-*tert*-butyl ((1,3,6,8-tetraoxo-1,3,6,8-tetrahydrobenzo[*lmn*][3,8]phenanthroline-2,7-diyl)bis(ethane-2,1-diyl))dicarbamate (NDIEAB) intermediate (1.7 g, 83%) as an orange solid. HI (1.67 mL, 12.6 mmol, 57%) was added to a suspension of the intermediate (1.7 g, 3.08 mmol) in EtOH (15 mL) at 0 °C. The mixture was stirred for 12 h and the solution concentrated, resuspended in diethyl ether (10 mL), filtered, washed with diethyl ether and isopropanol, and vacuum-dried to yield NDIEAI₂ (0.7 g, 75%) as a yellow solid. ¹H NMR (400 MHz, (CD₃)₂SO): δ = 8.74 (s, 4H), 7.81 (s, 6H), 4.35 (t, *J* = 5.9 Hz, 4H), 3.20 (q, *J* = 5.9 Hz, 4H) ppm; ¹³C NMR (101 MHz, (CD₃)₂SO): δ = 163.73, 130.88, 127.06, 126.68, 38.35, 37.98 ppm; HRMS (ESI+/QTOF): *m/z* (%) 353.1241 (100, [M]⁺, calcd for C₁₈H₁₇N₄O₄⁺: 353.1244); (ESI-/QTOF): *m/z* (%) 126.9055 (100, [M]⁻, calcd for I⁻: 126.9050).

Perovskite mechanosynthesis: Perovskite powders were synthesized by grinding the reactants in an electric ball mill (Retsch Ball Mill MM-200) using a grinding jar (10 ml) and a ball (∅10 mm) for 30 min at 25 Hz in accordance with the previously reported procedure.^[1-2] The amounts of reagents taken into the synthesis were determined by the reported stoichiometry. The resulting powders were annealed at 150 °C for 15 min to reproduce the thin-film synthetic procedure.

Thin film preparation: Films were fabricated through a stepwise preparation process. The substrates were cleaned with oxygen plasma for 15 min. The precursor solution of the (NDIEA)FA_{*n*-1}Pb_{*n*}I_{3*n*+1} (NDIEA = 2,2'-(1,3,6,8-tetraoxo-1,3,6,8-tetrahydrobenzo[*lmn*][3,8]phenanthroline-2,7-diyl)bis(ethan-1-aminium)) layered perovskite films (*n* = 1, 2, 3) of the defined concentration (0.4–0.6 M) was prepared by dissolving the stoichiometric quantities of PbI₂, FAI, and NDIEA₂ in the solvent mixture comprised of dimethylformamide (DMF) and dimethylsulfoxide (DMSO) with the volume ratio of 4:1. The perovskite film was deposited by spin-coating onto the substrate. The spin-coating procedure was performed in a glovebox under inert nitrogen atmosphere by a consecutive two-step spin-coating process at first 1000 rpm for 10 s with a ramp of 200 rpm s⁻¹ and second 4000 rpm for 20 s with a ramp of 2000 rpm s⁻¹. Subsequently, the substrate was annealed at 150 °C for 15 min.^[1]

UV-Vis absorption measurements were recorded using Varian Cary5 UV–visible spectrophotometer.

Steady-state photoluminescence (PL) spectra were recorded by exciting the layered perovskite films deposited onto microscope glass. The emission between 460–830 nm was recorded with a Fluorolog 322 spectrometer (Horiba Jobin Yvon iHr320 and a CCD) within with a bandpass of 5 nm upon

excitation at 420 nm with a band pass of 5 nm. The samples were mounted at 60° and emission recorded at 90° from the incident beam path.

X-ray diffraction (XRD) patterns were recorded on an X'Pert MPD PRO (PANalytical) equipped with a ceramic tube providing Ni-filtered (Cu anode, $\lambda = 1.54060 \text{ \AA}$) radiation and a RTMS X'Celerator (PANalytical). The measurements were done in BRAGG-BRENTANO geometry. The samples were mounted without further modification and the automatic divergence slit (10 mm) and beam mask (10 mm) were adjusted to the dimension of the films.

S2. Supplementary NMR Data

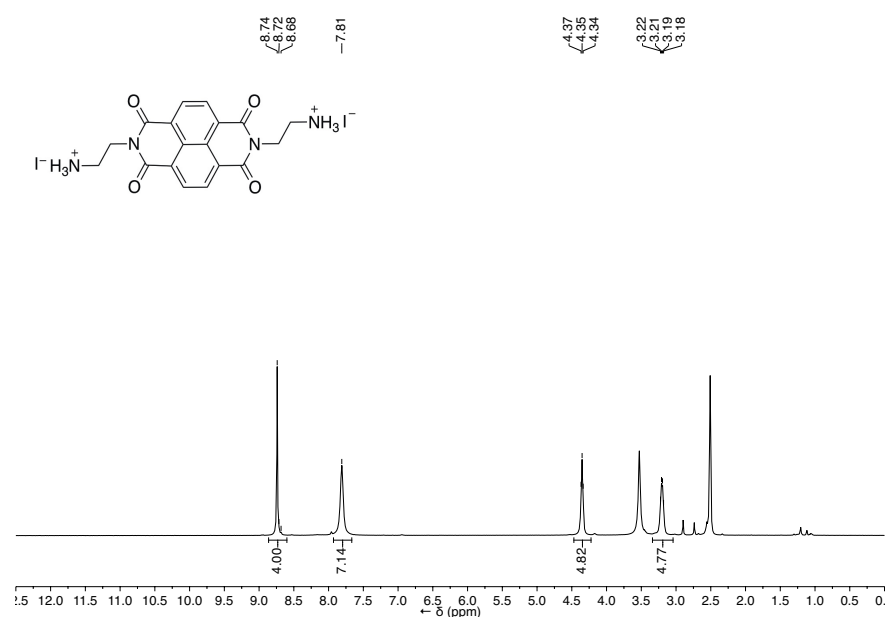


Figure S1. ¹H NMR of NDIEAI₂ in (CD₃)₂SO (400 MHz, 298 K)

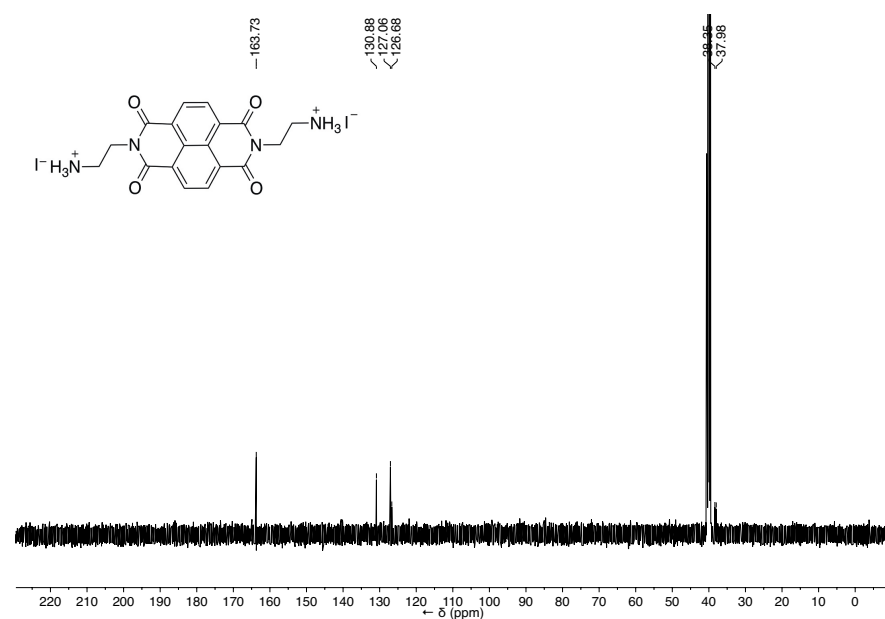


Figure S2. ¹³C NMR of NDIEAI₂ in (CD₃)₂SO (101 MHz, 298 K)

S3. Molecular Dynamics Simulations

S3.1. MD Methods

The initial structures were built with VMD by placing the ligands between layers of Pb—I octahedra. A fixed-point charge interatomic potential was chosen for Pb and I from the available literature.^[6] We have selected this force field as it is known to represent the crystal structures of both PbI₂ and perovskites. The Generalized Amber Force Field (GAFF) was used to parameterize the ligand and formamidinium ions. The force field files are available upon request from the corresponding author. We have chosen a 1.0 nm cutoff for nonbonded interactions and three-dimensional periodic boundary conditions were applied for each simulation. Long-range electrostatic interactions were treated with the particle-particle-particle-mesh Ewald method. We employed the SHAKE algorithm^[7] to constrain the bond length of hydrogen atoms. The time step used in all of the simulations was 2 fs. The simulations were performed with the Large-scale Atomic/Molecular Massively Parallel Simulator (LAMMPS) code.^[8] The systems were first minimized with a conjugate gradient algorithm with a tolerance of maximum residual force of 10⁻³ kcal/molÅ. After minimization, the systems were relaxed with an equilibrium run which was carried out in the isothermal-isobaric ensemble. We used a velocity rescaling thermostat with a relaxation time of 0.1 ps.^[9] The Parrinello-Rahman barostat^[10] was used to keep the pressure equal to the standard atmospheric pressure. The relaxation time of the barostat was set to 10 ps. We use the triclinic variable cell barostat in all of our simulations. With this setup, the temperature was slowly increased from 0 K to T (specified temperature) in 10 ns. We then performed 30 ns simulations at the constant temperature. The resulting structures obtained by MD simulations were further used as input structures for DFT optimizations (Section S4).

S3.2. Structure Analysis

Predicting crystal structures of mixed organic-inorganic multi-component perovskites is a complex problem. In particular, the high level of complexity in this case stems from the larger size and multifunctional structure of the spacer molecules, which can have multiple bonding arrangements. To simplify the problem, we limited our study to the 2D perovskite space. We started initially from a smaller supercell with Dion-Jacobson structure by placing NDIEA molecules between layers of corner-sharing Pb—I octahedra and follow a similar protocol as in our previous studies.^[6] The structural evolution from the initial guess to the final (lowest-energy equilibrated structure) is shown in the Supplementary movie. We obtain stable 2D-perovskite structures for $n = 1-4$ composition from classical MD that were subsequently relaxed at the DFT level (Figure S3).

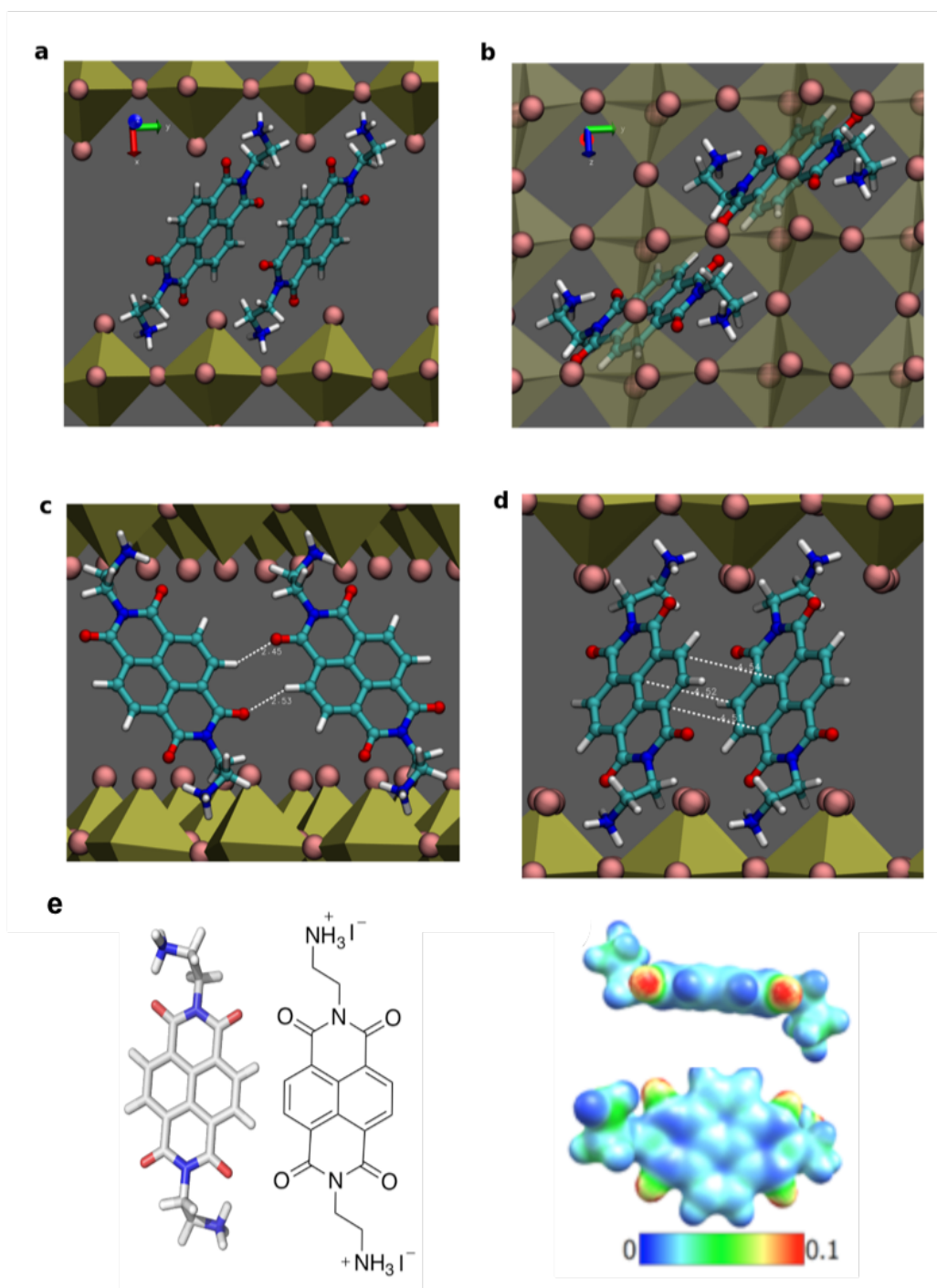


Figure S3. Structural analysis for 2D-NDIEA based perovskites. (a) Side view of the equilibrated geometry for $n = 1$ composition. (b) Inter-ligand arrangement. NDIEA molecules interact via (c) hydrogen bonding and (d) π - π interactions. Only two NDIEA molecules are represented for the sake of clarity. The images are generated with VMD. Pb—I octahedra are shown with golden color, iodide anions are depicted with orange spheres, whereas NDIEA molecules are shown with balls-and-sticks models: carbon is shown in light blue, nitrogen in dark blue, oxygen as red and hydrogen atoms in white. (e) Electrostatic potential surface map of unprotonated NDIEA spacer groups along with the corresponding structure and optimized geometry (DFT B3LYP/6-21G(d)) with a relative charge scale.

S4. DFT Calculations

S4.1. DFT Methods

Ab initio calculations based on the Generalized Gradient Approximation (GGA) of Density Functional Theory (DFT) were performed using the Quantum Espresso code.^[11] The Perdew–Burke–Ernzerhof functional revised for solids (PBEsol)^[12] was chosen based on benchmarks on 2D perovskites of AVA-MA^[13a] and AVA-FA^[14] where a good description of the electronic and structural properties was achieved with this functional. Valence-core electron interactions were taken into account using ultra-soft pseudopotentials in combination with a plane wave basis set up to kinetic energy cutoffs of 60 Ry and 350 Ry for the wavefunction and for the density, respectively. The Brillouin zone was sampled by $2 \times 2 \times 4$ and $1 \times 2 \times 4$ k-point grids for $n = 1, 2$ and $n = 3$, respectively. The Coulomb-Attenuation Method (CAM) in the form of the CAM-B3LYP functional^[15] was employed for calculation of the band gaps to reliably predict charge-transfer excitations with low orbital overlap, taking also the spin–orbit coupling (SOC) effects into account, which are calculated at the GGA level. For this, norm-conserving pseudopotentials were used with a plane wave basis set of 80 Ry kinetic energy cutoff for the wavefunctions. To verify the nature of the band edges, projected density of states for the frontier orbitals were obtained at the PBE0 level.^[16] Eventually, to compare the charge transfer features of these systems with other 2D and 2D/3D systems, effective masses of the charge carriers were determined via numerical differentiation of the band structures.^[13b]

S4.2. Structural Analysis

The structures were initially obtained by classical molecular dynamics simulations, equilibrated at the force-field level and later optimized at DFT level. Due to the bifunctional nature of NDIEA ligands, an initial Dion-Jacobson (DJ) phase was adopted and maintained in the final DFT-optimized structures (as depicted in Figure S4).

Figure S4. DFT (PBEsol) - optimized structure of (NDIEA)PbI₄. Definition of some characteristic structural parameters (d_1 , d_2) are indicated.

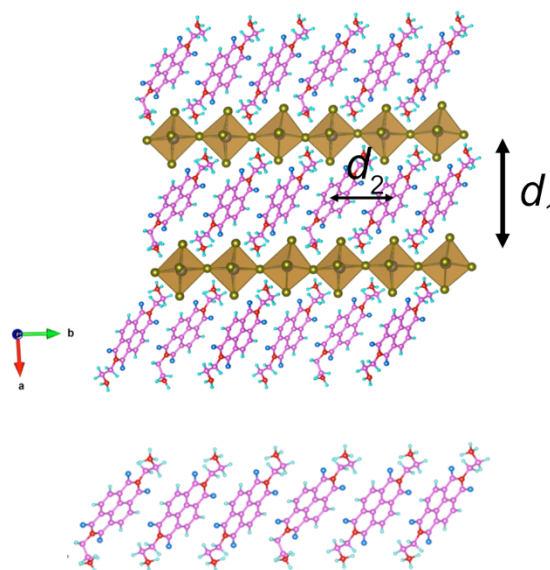


Table S1. Characteristic structural features of (NDIEA)FA_{n-1}Pb_nI_{3n+1} for $n = 1-3$. Octahedral tilting angles were measured with respect to two in-plane and one out-of-plane directions. Distances are given in angstrom. Angles of octahedral tilting, tilting of the aromatic planes with respect to the perovskite layer and corresponding standard deviations are in degrees.

| n | Octahedral Tilting (°) | N \cdots Pb (Å) | d_1 (Å) | d_2 (Å) | Spacer Tilting (°) |
|-----|--|-------------------|-----------|-----------|--------------------|
| 1 | 90.85 ± 8.13 88.09 ± 4.96 | 2.9 | 16.3 | 6.4 | 43.6 ± 1.9 |
| 2 | 90.6 ± 4.3 88.8 ± 4.0 83.3 ± 2.7 | 2.7 | 15.6 | 6.4 | 48.1 ± 3.1 |
| 3 | 89.8 ± 4.8 89.5 ± 5.0 88.0 ± 3.3 | 2.5 | 16.2 | 6.3 | 47.7 ± 0.2 |

S4.3. Electronic Properties

The band gaps for the optimized (NDIEA)FA_{n-1}Pb_nI_{3n+1} structures were calculated at the CAM-B3LYP level including SOC effects. The calculated band gap for (NDIEA)PbI₄ is 2.37 eV, which is in good agreement with the measured optical gap (2.0 eV; Table S1), given that the excitonic effects are not included in the calculations. In comparison to the band gaps of the (PDMA)FA_{n-1}Pb_nI_{3n+1} systems or other 2D perovskites,^[17] the band gap is systematically lower in the case of NDIEA spacers.^[18,19] This is the result of two effects: (1) The bottom of the conduction band (BCB) is localized on the NDIEA molecules, which leads to a significant lowering of the conduction band with respect to that in the PDMA-based or other systems with electro-inactive spacers,^[17] and (2) the structures of the inorganic slabs are more cubic, which enhances orbital overlap and destabilizes the top of the valence band (TVB).^[20] The NDIEA spacers adopt a preferred conformation, which remains essentially unchanged during 5 ps of ab-initio molecular dynamics simulations at finite temperatures of 200 K, 300 K and 400 K. The hole effective masses in the in-plane directions (Table S2) decrease as expected upon increasing n while significantly larger hole and electron masses are found for the direction perpendicular to the inorganic layer. In general, the in-plane hole effective masses are of the same order of magnitude as those of the other 2D perovskites, such as the PDMA-based structures.^[17] However, the same behavior is not observed for the electron effective masses as the BCB is localized on the NDIEA molecules.

Table S2. Calculated band gaps at CAM-B3LYP+SOC level together with hole (m_h) and electron (m_e) effective masses of (NDIEA)FA $_n$ -1Pb $_n$ I $_{3n+1}$ for $n=1, 2$ and 3 calculated at the GGA level. The available experimental values are indicated with an asterisk. Analogous effective masses for PDMA-based systems are indicated with #.

| n | Band gap (eV) | $m_{h,xx}$ | $m_{h,yy}$ | $m_{h,zz}$ | $m_{e,xx}$ | $m_{e,yy}$ | $m_{e,zz}$ |
|-----|---------------|-------------------------|-------------------------|------------|------------------------|-------------------------|------------|
| 1 | 2.37, 2.0* | 0.27, 0.30 [#] | 0.62, 0.34 [#] | Large | 6.7, 0.31 [#] | 90.0, 0.38 [#] | Large |
| 2 | 1.75, 1.6* | 0.18, 0.29 [#] | 0.29, 0.32 [#] | Large | 3.4, 0.12 [#] | 14.8, 0.81 [#] | Large |
| 3 | 1.74 | 0.18, 0.21 [#] | 0.23, 0.24 [#] | Large | 5.3, 0.12 [#] | 12.1, 1.18 [#] | Large |

Partial densities of states (Figure S5, a–c) indicate a contribution from the organic part to the band edges for $n = 1, 2$ and 3 perovskite compositions. Furthermore, frontier molecular orbitals (Figure S5, d–f) indicate localization of the BCB and higher states on the ligand, while the TVB is delocalized over the inorganic part.

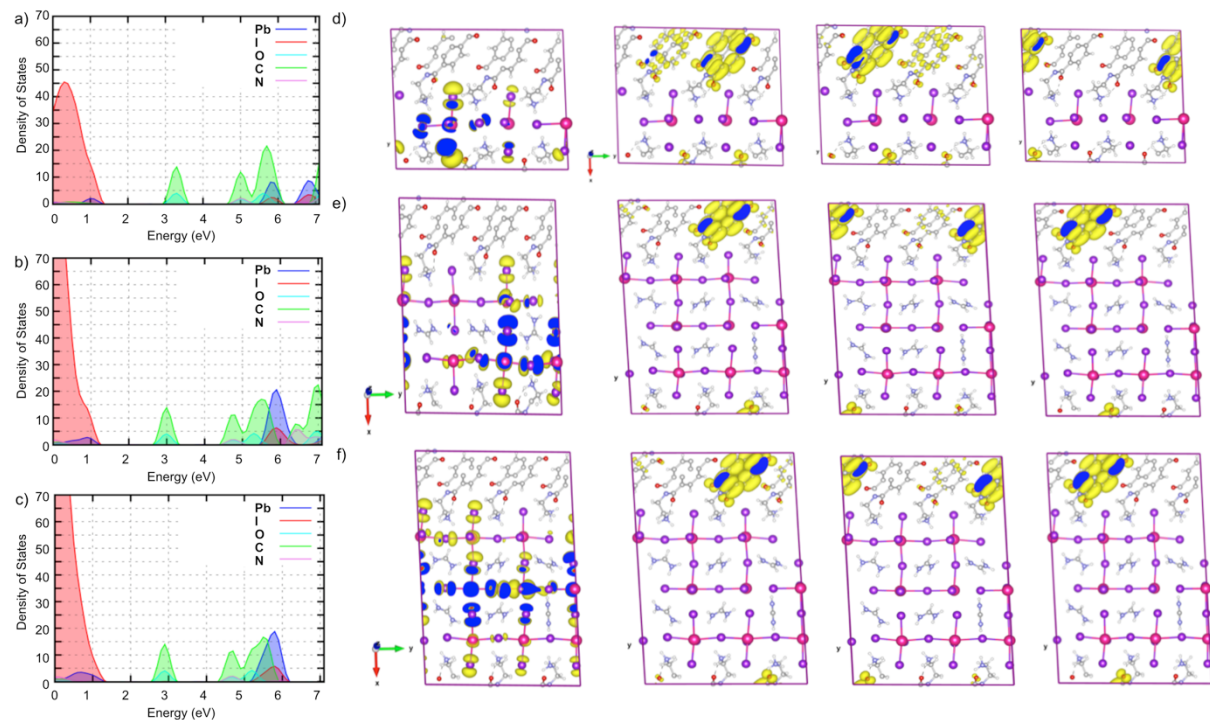


Figure S5. (a–c) Calculated partial densities of states at the PBE0 level of theory for (NDIEA)FA $_n$ -1Pb $_n$ I $_{3n+1}$, (a) $n = 1$, (b) $n = 2$, and (c) $n = 3$ compositions. (d–f) Frontier molecular orbitals (HOMO, LUMO, LUMO+1 and LUMO+2) at PBE0 level for (NDIEA)FA $_n$ -1Pb $_n$ I $_{3n+1}$ (d) $n = 1$, (e) $n = 2$ and (f) $n = 3$ compositions. (d–f) Frontier molecular orbitals (HOMO, LUMO, LUMO+1 and LUMO+2) at PBE0 level for (NDIEA)FA $_n$ -1Pb $_n$ I $_{3n+1}$ (d) $n = 1$, (e) $n = 2$ and (f) $n = 3$ compositions.

S5. X-Ray Scattering Measurements

S5.1. Methods

Grazing incidence wide angle X-ray scattering of (NDIEA)FA_{n-1}Pb_nI_{3n+1} thin films on glass slides was measured at 2° incidence angle with a D8 Discover Plus TXS (Bruker) equipped with rotating anode (Cu), a Dectris Eiger2 2D detector, and using a point-collimated beam of approx. 300 μm, at a power of 5.4 kW.

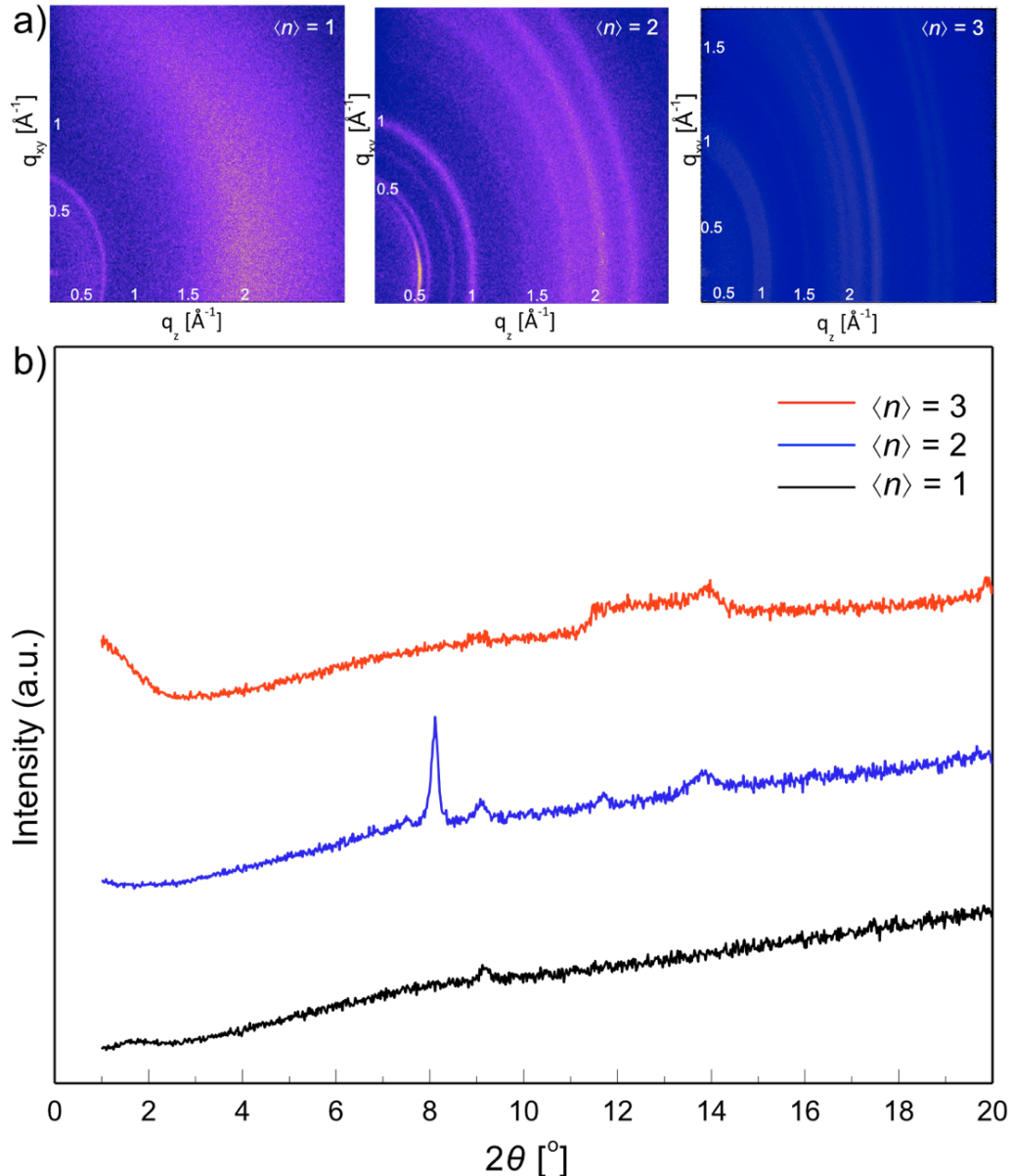


Figure S6. (a) Grazing incidence wide angle X-ray scattering (GIWAXS) data at incidence angles of ca. 2° and the corresponding (b) XRD patterns for thin films of (NDIEA)FA_{n-1}Pb_nI_{3n+1} ($\langle n \rangle = 1-3$) compositions on microscope glass. Integrated diffraction patterns (from 2D GIWAXS images) for thin films of (NDIEA)FA_{n-1}Pb_nI_{3n+1} ($\langle n \rangle = 1-2$) compositions on microscope glass slides are provided in the main manuscript (Figure 3c).

S6. Transient Absorption Spectroscopy

S6.1. Methods

Transient absorption spectroscopy measurements were performed on thin-films of perovskite materials of $(\text{NDIEA})\text{FA}_{n-1}\text{Pb}_n\text{I}_{3n+1}$ ($\langle n \rangle = 1-2$) compositions along with a neat spacer material. In addition, a reference Dion-Jacobson system based on a $(\text{PDMA})\text{PbI}_4$ composition comprising electronically inactive 1,4-phenylenedimethan ammonium (PDMA) organic spacer was analyzed for comparison.

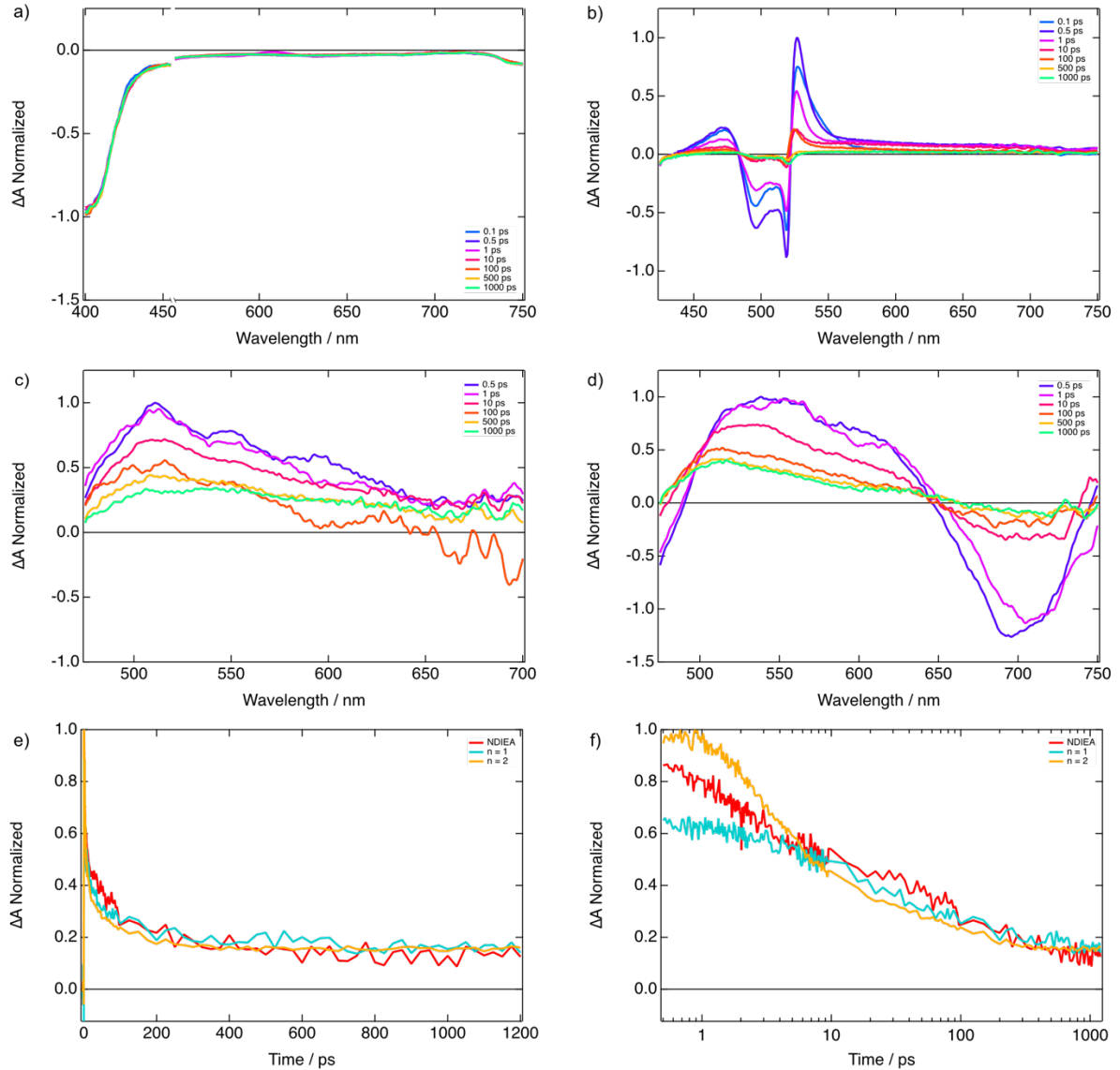


Figure S7. Transient absorption spectra for control thin films of $(\text{PDMA})\text{PbI}_4$ composition upon excitation at (a) 510 nm and (b) 390 nm. The bleach at around 500 nm observed under b) is characteristic for layered hybrid perovskites of $n = 1$ composition. The spectral characteristics upon excitation at 510 nm shown in a) are different from those of the $(\text{NDIEA})\text{FA}_{n-1}\text{Pb}_n\text{I}_{3n+1}$ ($\langle n \rangle = 1-2$) compositions shown in the main manuscript in accordance with different electronic properties. (c–d) Transient absorption spectra for thin films of $(\text{NDIEA})\text{FA}_{n-1}\text{Pb}_n\text{I}_{3n+1}$ ($\langle n \rangle = 1-2$) compositions upon excitation at 450 nm. (e–f) Temporal evolution of the main absorption (530 nm) for NDIEAI_2 (red) and $(\text{NDIEA})\text{FA}_{n-1}\text{Pb}_n\text{I}_{3n+1}$ ($\langle n \rangle = 1$ in blue and $\langle n \rangle = 2$ in orange), revealing different dynamics as a function of the composition.

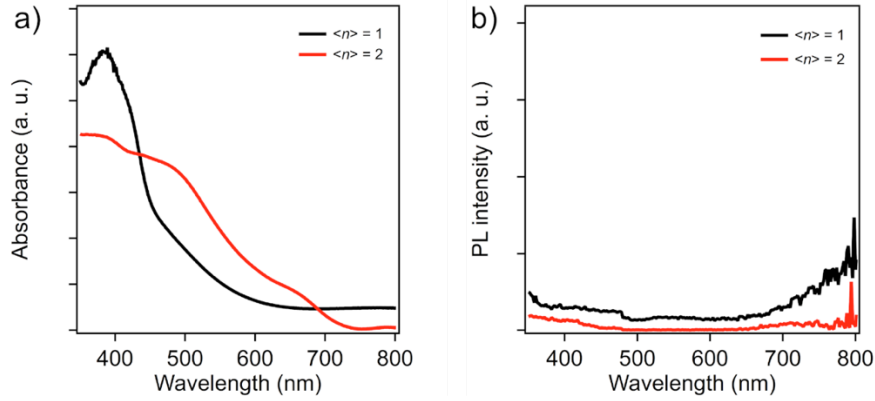


Figure S8. (a) UV-vis absorption and (b) steady-state photoluminescence (PL) spectra of thin films of (NDIEA)FA_{n-1}Pb_nI_{3n+1} ($\langle n \rangle = 1$ in black and $\langle n \rangle = 2$ in red) compositions upon excitation at 420 nm. The preparation of the films is detailed in the Methods section, whereas the concentration of both precursors' solutions for $\langle n \rangle = 1-2$ compositions was 0.4 M.

S7. Time Resolved Microwave Conductivity Measurements

S7.1. Methods

Time-resolved microwave conductivity (TRMC) measurements were used to probe changes in conductivity of layered hybrid perovskites was probed by using high frequency microwaves after the excitation by either high energy electron pulse or a laser.^[21-22] The generated free charge carriers absorb part of the microwave power and the fraction of the incoming microwave power absorbed by the sample (ΔG) is proportional to the change in conductivity of the material ($\Delta\sigma$), which is defined as the product of charge mobility (μ) and quantum yield of free charge carrier formation (φ). Therefore, from the maximum change in conductivity ($\Delta\sigma_{\max}$), mobility (μ) and quantum yield of free charge carrier formation (φ) can be obtained. The relative mobility of charge carriers was estimated by *pulse-radiolysis TRMC*. *TRMC upon laser photoexcitation* under conditions specified in the corresponding figure captions was used to analyze *thin films* of approximately 200 nm thickness of the layered perovskite materials based on different composition ($\langle n \rangle = 1-3$) as reported (Figure S9).

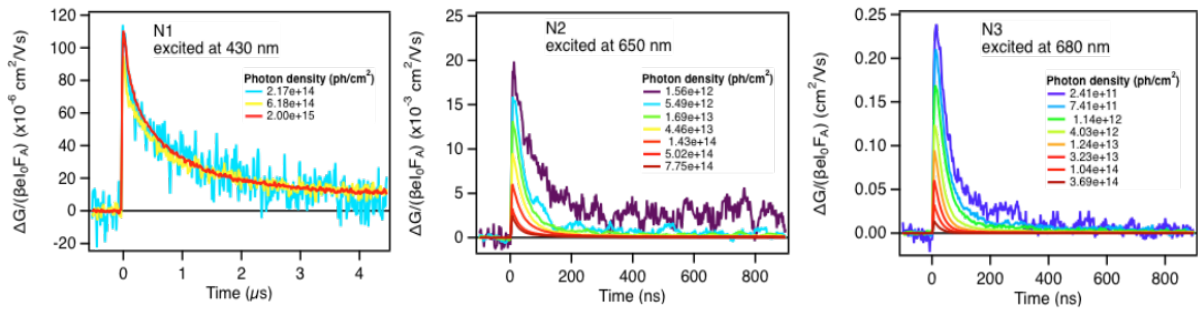


Figure S9. Evolution of photoconductivity over time upon excitation of different perovskite compositions ($\langle n \rangle$) with various photon intensities (cm^{-2}) at 293 K for $\langle n \rangle = 1$ (excitation at 430 nm), $\langle n \rangle = 2$ (excitation at 650 nm), and $\langle n \rangle = 3$ (excitation at 680 nm) compositions.

S8. Photovoltaic Performance

S8.1. Materials

Commercial materials were used in the process: titanium diisopropoxide bis(acetylacetonate) (75 wt% in isopropanol, Sigma-Aldrich); anhydrous ethanol (99.5%, Fischer Scientific); TiO₂ paste (Dyesol 30 NR-D); tin(IV) oxide colloidal dispersion (15% in water, Alfa Aesar); nickel nitrate hexahydrate (Ni(NO₃)₂·6H₂O, 99.99%, Sigma Aldrich); 2-methoxyethanol (99%, Roth); [6,6]-Phenyl-C₆₁-butyric acid methyl ester (PC₆₀BM, Sigma Aldrich); chlorobenzene (99.8%, ACROS); bathocuproine (98%, TCI); Spiro-OMeTAD (99%); lithium bis(trifluoro-methylsulphonyl)imide (Li-TFSI, 99.95%, Sigma Aldrich); 4-*tert*-butylpyridine (4-*t*BP, 96%, Sigma-Aldrich); lead iodide (PbI₂, 99.9985%, Alfa Aesar); formamidinium iodide (FAI, 398%, Greatcellsolar); methylammonium iodide (MAI, 398%, Greatcellsolar); methylammonium chloride (MACl, 99%, Dyenamo); dimethylformamide (DMF, 99.8%, Acros); dimethyl sulfoxide (DMSO, 99.7%, Acros).

S8.2. Methods

Compact blocking TiO₂ layer (c-TiO₂): A ca. 40 nm-thick TiO₂ compact layer (c-TiO₂) was deposited by spray pyrolysis with a precursor solution of titanium diisopropoxide bis(acetylacetonate) (75 wt% in isopropanol, Sigma-Aldrich) in anhydrous ethanol (99.5%, Fischer Scientific) at 450 °C. After spraying, the substrates were kept at 450 °C for 30 min.

Mesoscopic TiO₂ layer (m-TiO₂): A suspension of TiO₂ paste (Dyesol 30 NR-D) in ethanol (1:6 wt/wt) was used to cast a ca. 250 nm-thick mesoporous TiO₂ layer by spin coating at 4000 rpm for 20 s. After the spin coating, the solvent was allowed to evaporate on a hot plate at 80 °C for 10 min and then sintered at 450 °C for 30 min under dry air flow.

SnO₂ layer: A 15% tin (IV) oxide colloidal dispersion in water (Alfa Aesar) was further diluted in dionized water (1:6 v/v). The dispersion was spin coated over the substrates at 5000 rpm during 25 s followed by annealing at 160 °C for 30 min in ambient air.

NDIEA-treated-SnO₂: A 1 mM NDIEAI₂ solution in DMSO was used to treat the surface of the SnO₂ layers in some devices. The solution was spin-coated onto the substrates at 4000 rpm for 20 s and then the films were heated to 100 °C for 10 min.

NiO_x layer: A 0.1 M Ni(NO₃)₂·6H₂O (Sigma Aldrich, 99.99%) in 2-methoxyethanol (Roth, 99%) was prepared in an argon filled glovebox and stirred overnight at room temperature. The substrates were then spin-coated from solution at 4000 rpm for 20 s and annealed at 500 °C for 30 min in ambient air.

PC₆₀BM: A 22 mM PC₆₀BM (Sigma Aldrich) solution in chlorobenzene was deposited on the perovskite substrate by spin-coating at 4000 rpm for 30 s. A heat treatment was carried out at 100 °C for 10 min in dry air.

Bathocuproine (BCP): A bathocuproine (TCI, 98.0%) solution (0.5 mg/1 mL ethanol) was deposited on top of PC₆₀BM by spin-coating at 6000 rpm for 20 s in dry air.

Spiro-OMeTAD: A solution of Spiro-OMeTAD (73.5 mM) in chlorobenzene with Li-TFSI (37 mM) and 4-*t*BP (0.24 M) was casted over the perovskite by spin-coating at 4000 rpm for 20 s in dry air.

(NDIEA)FA₂Pb₃I₇ (n = 3 system): A solution of 1.2 M PbI₂ (Alfa Aesar), 0.8 M FAI (Greatcell) and 0.4 M NDI in DMF/DMSO (4:1 v/v) was casted by spin-coating at 5000 rpm for 20 s followed by an annealing process at 150 °C for 20 min in dry air.

FAPbI₃: We followed a two-step deposition solution process, analogous to the one previously reported,^[23] a solution of 1.3 M PbI₂ in DMF:DMSO (9.5:0.5 v/v) was spin coated at 1500 rpm for 30 s,

and then annealed at 70 °C for 1 min in a dry atmosphere, subsequently, a solution of FAI:MAI:MACl (60 mg: 8.5 mg: 6 mg in 1 mL isopropanol) was spin coated at 2000 rpm for 20 s, and was then annealed at 150 °C for 15 min in ambient air (of 30–40% relative humidity).

NDIEA-infiltrated FAPbI₃ (FAPbI₃:NDIEAI₂): The exact same procedure as for the FAPbI₃ films was followed with the only difference being that 1mM NDIEAI₂ was added to the PbI₂ solution.

The solar cell devices were prepared over glass substrates covered by fluorine-doped tin oxide (FTO) (Nippon sheet glass 8 W·sq⁻¹). Standard cleaning process was performed of the substrates before film deposition; the substrates were thoroughly brushed with a 10% Hellmanex (Hellma GmbH) solution and then sequentially sonicated in a 2% Hellmanex solution, acetone and ethanol for 30, 15 and 10 min, respectively. Additionally, the substrates were treated under UV-Ozone for 15 min between every layer before the perovskite deposition, with the exception of the p-i-n devices where there was no UV-Ozone treatment on the NiO_x deposition. The architectures are summarized in Table S3.

Table S3. Summary of different device architectures employed in this study

| | | |
|-----------|----|--|
| 2D | M1 | n-i-p mesoscopic (Glass/FTO/c-TiO ₂ /m-TiO ₂ /(NDIEA)FA ₂ Pb ₃ I ₇ /Spiro-OMeTAD) |
| | M2 | n-i-p planar (Glass/FTO/c-TiO ₂ /SnO ₂ /(NDIEA)FA ₂ Pb ₃ I ₇ /Spiro-OMeTAD) |
| | M3 | p-i-n planar (Glass/FTO/NiO _x /(NDIEA)FA ₂ Pb ₃ I ₇ /PCBM/BCP) |
| 3D | M1 | n-i-p planar (Glass/FTO/c-TiO ₂ /SnO ₂ /FAPbI ₃ :NDI/Spiro-OMeTAD) |
| | M2 | n-i-p planar (Glass/FTO/c-TiO ₂ /NDIEAI ₂ -treated-SnO ₂ /FAPbI ₃ /Spiro-OMeTAD) |

S8.3. Supplementary Data

Table S4. Summary of average performance metrics for 2D perovskite compositions

| Architecture | V _{oc} (V) | J (mA cm ⁻²) | FF | PCE (%) |
|--------------|---------------------|--------------------------|------|---------|
| M1 | 0.406 | 0.01942 | 0.41 | 0.003 |
| M2 | 0.426 | 0.02425 | 0.42 | 0.004 |
| M2* | 0.458 | 0.11965 | 0.39 | 0.021 |
| M3* | n.a. | 0.04485 | n.a. | n.a. |

Note that * refers to half the concentration described in the methods section.

Table S5. Summary of average performance metrics for 3D perovskite compositions

| Architecture | V _{oc} (V) | J (mA cm ⁻²) | FF | PCE (%) |
|--------------|---------------------|--------------------------|------|---------|
| M1 | 0.727 | 8.6 | 0.47 | 2.95 |
| M2 | 0.854 | 22.9 | 0.58 | 11.32 |

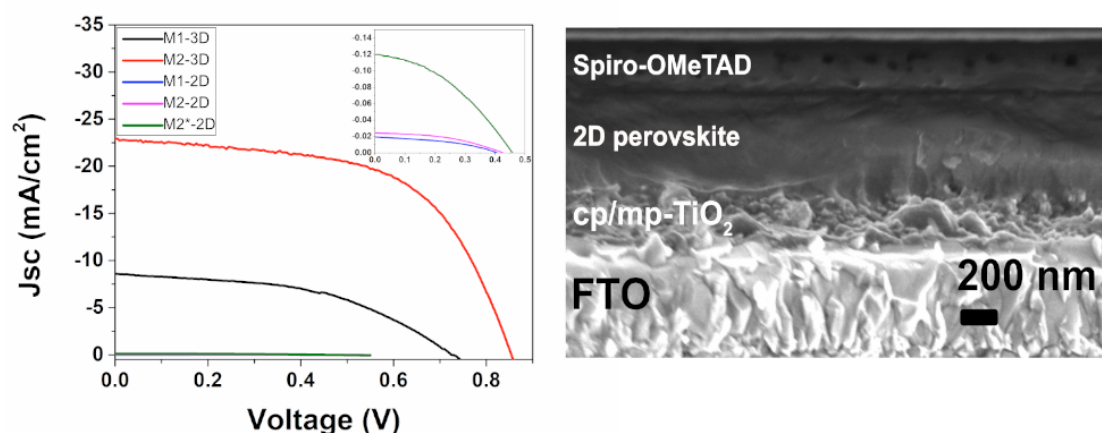


Figure S10. Left: Representative J - V curves for devices prepared by using J conditions summarized in Table S3 recorded under standard AM 1.5G illumination at a light intensity of 100 mW cm⁻² at a scanning rate of 50 mV s⁻¹ under standard AM 1.5G solar radiation and reverse bias (from V_{OC} to J_{SC}). Right: Cross-sectional SEM image of a representative (NDIEA)FA₂Pb₃I₁₀-based device.

References

- [1] Y. Li *et al.*, Bifunctional Organic Spacers for Formamidinium-Based Hybrid Dion–Jacobson Two-Dimensional Perovskite Solar Cells. *Nano Lett.* **19**, 150–157 (2019)
- [2] J. V. Milić *et al.*, Supramolecular Engineering for Formamidinium-Based Layered 2D Perovskite Solar Cells: Structural Complexity and Dynamics Revealed by Solid-State NMR Spectroscopy. *Adv. Energy Mater.* **131**, 1900284 (2019)
- [3] P. Gratia *et al.*, The Many Faces of Mixed Ion Perovskites: Unraveling and Understanding the Crystallization Process, *ACS Energy Lett.* **12**, 2686–2693 (2017)
- [4] J-H. Im *et al.*, 6.5% Efficient Perovskite Quantum-Dot-Sensitized Solar Cell, *Nanoscale* **3**, 4088–4093 (2011)
- [5] D. J. Kubicki *et al.*, Phase Segregation in Cs-, Rb- and K-Doped Mixed-Cation (MA)_x(FA)_{1-x}PbI₃ Hybrid Perovskites from Solid-State NMR. *J. Am. Chem. Soc.* **139**, 14173–14180 (2017)
- [6] C. Caddeo *et al.*, Collective Molecular Mechanisms in the CH₃NH₃PbI₃ Dissolution by Liquid Water. *ACS Nano* **11**, 9183–9190 (2017)
- [7] J.-P. Ryckaert *et al.*, Numerical Integration of the Cartesian Equations of Motion of a System with Constraints: Molecular Dynamics of n-Alkanes. *J. Comput. Phys.* **23**, 327–341 (1977)
- [8] S. Plimpton, Fast Parallel Algorithms for Short-Range Molecular Dynamics. *J. Comput. Phys.* **117**, 1–19 (1995)
- [9] G. Bussi *et al.*, Canonical Sampling Through Velocity Rescaling. *J. Chem. Phys.* **126**, 014101 (2007)
- [10] M. Parrinello, and A. Rahman, Polymorphic Transitions in Single Crystals: A New Molecular Dynamics Method. *J. Appl. Phys.* **52**, 7182–7190 (1981)
- [11] P. Giannozzi *et al.*, QUANTUM ESPRESSO: A Modular and Open-Source Software Project for Quantum Simulations of Materials. *J. Phys.: Condens. Matter* **21**, 395502–395502 (2009)
- [12] J. P. Perdew *et al.*, Restoring the Density-Gradient Expansion for Exchange in Solids and Surfaces. *Phys. Rev. Lett.* **100**, 136406–136406 (2008)
- [13] (a) N. Ashari-Astani *et al.*, Ruddlesden–Popper Phases of Methylammonium-Based Two-Dimensional Perovskites with 5-Ammonium Valeric Acid AVA₂MA_{n-1}Pb_nI_{3n+1} with n = 1, 2, and 3. *J. Phys. Chem. Lett.* **10**, 3543–3549 (2019); (b) A.-A. Negar *et al.*, Computational Characterization of the Dependence of Halide Perovskite Effective Masses on Chemical Composition and Structure. *J. Phys. Chem. C.* **121**, 23886–23895 (2017)
- [14] A. Q. Alanazi *et al.*, Atomic-Level Microstructure of Efficient Formamidinium-Based Perovskite Solar Cells Stabilized by 5-Ammonium Valeric Acid Iodide Revealed by Multi-Nuclear and Two-Dimensional Solid-State NMR. *J. Am. Chem. Soc.* **141**, 17659–17669 (2019)
- [15] T. Yanai *et al.*, A New Hybrid Exchange-Correlation Functional Using the Coulomb-Attenuating Method (CAM-B3LYP). *Chem. Phys. Lett.* **393** 51–57 (2004)
- [16] C. Adamo and V. Barone, Toward Reliable Density Functional Methods Without Adjustable Parameters: The PBE0 Model. *J. Chem. Phys.* **110**, 6158–6170 (1999)
- [17] F. Jahanbakhshi *et al.*, Organic Spacers in 2D Perovskites: General Trends and Structure-Property Relationships from Computational Studies. *Helv. Chim. Acta* **104**, e2000232 (2021)
- [18] S. Ahmad *et al.*, Dion-Jacobson Phase 2D Layered Perovskites for Solar cells with Ultrafast Stability, *Joule* **3**, 1–3 (2018)
- [19] J.-C. Blancon *et al.*, Extremely Efficient Internal Exciton Dissociation through Edge States in Layered 2D Perovskites, *Science* **355**, 1288–1292 (2017)
- [20] S. Meloni *et al.*, Valence and Conduction Band Tuning in Halide Perovskites for Solar Cell Applications' *J. Mater. Chem. A* **4**, 15997–16002 (2016)
- [21] R. Herckens *et al.*, Multi-Layered Hybrid Perovskites Templated with Carbazole Derivatives: Optical Properties, Enhanced Moisture Stability and Solar Cell Characteristics. *J. Mater. Chem. A.* **6**, 22899–22908 (2018)
- [22] M. C. Gélvez-Rueda *et al.*, Interconversion between Free Charges and Bound Excitons in 2D Hybrid Lead Halide Perovskites. *J. Phys. Chem. C.* **121**, 26566–26574 (2017)
- [23] Jiang *et al.*, Planar-Structure Perovskite Solar Cells with Efficiency beyond 21%. *Adv. Mater.* **29**, 1703852 (2017)